Master thesis and internship[BR]- Master's thesis : Modeling and control of active seismic isolation systems with non-minimum phase zeros for gravitational wave detectors[BR]- Integration internship

Auteur : Bertoglia, Massimo
Promoteur(s) : Collette, Christophe; Sacré, Pierre
Faculté : Faculté des Sciences appliquées
Diplôme : Master en ingénieur civil en aérospatiale, à finalité spécialisée en "aerospace engineering"
Année académique : 2024-2025
URI/URL : http://hdl.handle.net/2268.2/23300

UNIVERSITE DE LIEGE
FACULTE DES SCIENCES APPLIQUEES

Modeling and control of active seismic isolation systems with non-minimum phase zeros for gravitational wave detectors

Bertoglia Massimo

Thesis presented to obtain the degree of :
Master of science in aerospace engineering

Thesis supervisor :
Collette Christophe
Sacré Pierre

Academic year: **2024 - 2025**

Acknowledgments

I would first like to express my deepest gratitude to my thesis supervisors, Prof. Christophe Collette and Prof. Pierre Sacré, for their guidance, availability, and trust throughout this research. Their feedback, expertise, and vision have been invaluable in shaping the direction of this work.

I am especially thankful to Thomas Giordano, Haidar Lakkis, and Anthony Amorosi for their generous and tireless help. Their technical support, insightful discussions, and willingness to spend countless hours with me had a direct impact on the progress and quality of this project.

I would also like to warmly thank the entire team at the Precision Mechatronics Laboratory. Their enthusiasm, encouragement, and collaborative spirit made my internship a truly enriching experience, both professionally and personally.

Lastly, I would like to thank my parents and close friends for their unwavering support throughout my academic years. I am also deeply grateful to my partner for her patience and support during the final and most demanding months of this thesis. Without all of you, this achievement would not have been possible.

Abstract

This thesis investigates the origin of non-minimum phase zeros in the control of seismic isolation platforms, with a particular focus on gravitational wave detectors such as LIGO, Virgo and Einstein Telescope. These detectors require extreme precision, and even small parasitic dynamic effects can severely impair their sensitivity. Through a combination of analytical modeling, numerical simulations using MATLAB Simscape, and experimental validation, this study explores how the location and configuration of sensors and actuators affect the appearance and nature of transmission zeros. The results highlight the importance of structural geometry in mitigating tilt-horizontal coupling and show that careful sensor placement and mechanical decoupling are essential to achieving effective active control. The findings contribute to improving the robustness and bandwidth of control systems in next-generation detectors, with potential applications in other high-precision engineering systems.

Contents

List of Figures

List of Tables

Introduction

Gravitational wave astronomy has opened a new observational window into the universe, enabled by detectors that can measure displacements smaller than a proton's diameter. These detectors such as Advanced LIGO, Virgo, and KAGRA rely on interferometric techniques combined with elaborate vibration isolation systems. However, the presence of non-minimum phase zeros, caused by parasitic coupling between translation and tilt, limits the achievable performance of active isolation platforms. Understanding and mitigating these effects is critical for the development of more sensitive detectors.

This thesis aims to study the dynamics of active isolation platforms and analyze how mechanical configuration influences their controllability. Particular attention is paid to the transmission zeros of the system and how they can be shifted or suppressed through design. Using both numerical simulation and physical experiments, it aims to validate the theoretical findings and provide practical insights for engineering design.

Chapter 1

State of the art

1.1 Gravitational waves

Gravitational waves are distortions of space-time, analogous to ripples propagating through a flexible space-time continuum. They are generated by the presence and motion of massive accelerating objects [7]. Such waves are typically produced by cataclysmic astrophysical events, including black hole mergers, neutron star collisions, or processes from the early universe such as the Big Bang [8].

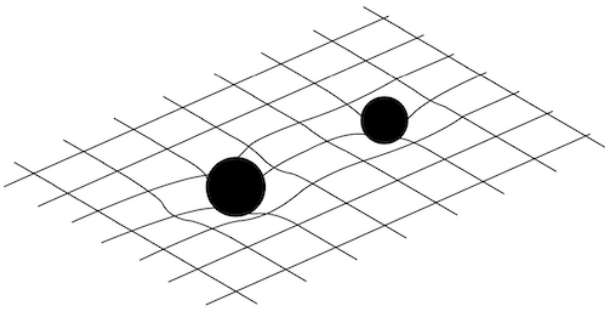

Figure 1.1: Illustration of space-time distortion [1]

First predicted in 1916 by Albert Einstein as a consequence of general relativity, gravitational waves constitute a direct manifestation of the dynamic curvature of space-time [7]. Despite their theoretical significance, the amplitude of these perturbations is exceedingly small, rendering them undetectable through conventional instrumentation. Their observation required the development of revolutionary measurement techniques and unprecedented levels of experimental precision [9]. Gravitational waves provide a unique observational window into astrophysical phenomena that are otherwise inaccessible via electromagnetic astronomy. Unlike electromagnetic waves, they propagate virtually unimpeded through matter, thus serving as unaltered messengers of the most extreme astrophysical events [10].

1.2 Need of precise control

Detecting gravitational waves is a formidable technical challenge. As these ripples in spacetime are incredibly faint, the instruments designed to detect them must achieve extraordinarily high levels of sensitivity and noise isolation. Gravitational waves cause infinitesimal changes in distance, on the order of one part in 10^{-19} m, comparable to measuring a shift smaller than a proton's diameter across several kilometers [11]. Capturing such minuscule distortions necessitates state-of-the-art experimental approaches.

The most successful method currently in use is laser interferometry. Pioneering facilities such as LIGO (Laser Interferometer Gravitational-Wave Observatory) in the United States and Virgo in Europe employ laser beams traveling through perpendicular arms several kilometers in length. By analyzing the interference pattern resulting from the recombination of these beams, it becomes possible to detect the incredibly small path-length variations induced by passing gravitational waves [3, 12].

(a) LIGO detector in Livingston (b) Virgo detector in Italy

Figure 1.2: Aerial views of the LIGO and Virgo detectors [2].

Other experimental strategies are also under active development:

- **Space-based interferometers** such as LISA (Laser Interferometer Space Antenna) aim to eliminate terrestrial seismic and thermal noise by operating in a quiet orbital environment [5].
- **Pulsar timing arrays** monitor the highly regular radio emissions from millisecond pulsars to detect timing residuals induced by gravitational waves [13].
- **Resonant bar detectors**, although historically pioneering, have largely been superseded by interferometric methods due to their lower sensitivity [14].

Each of these detection methods presents distinct technological challenges, particularly related to the suppression and characterization of noise sources that can mask or mimic gravitational-wave signals [15].

The first direct detection of a gravitational wave, announced by LIGO in 2015 and attributed to the merger of two stellar-mass black holes, marked a pivotal moment in modern

astrophysics. This event validated decades of theoretical work and experimental development, opening the era of gravitational-wave astronomy [11]. Today, international efforts continue to enhance detector sensitivity and broaden the global observatory network, with next-generation projects such as the Einstein Telescope and the Cosmic Explorer aiming to probe deeper into the gravitational-wave universe [16, 17].

1.3 Gravitational detectors

This section focuses on the mechanical isolation systems and control techniques that improve sensitivity, with particular emphasis on their implementation in the leading detectors: Advanced LIGO, GEO600, Advanced Virgo, KAGRA and also with a short regard on futur as Einstein telescope and LISA.

Ground-based gravitational wave detectors rely on a range of advanced technologies including laser optics, thermal management, and quantum noise reduction. The core working principle is that of a Michelson interferometer, as illustrated in Fig. 1.3. When a gravitational wave passes through the detector, it causes space-time to stretch and compress, which shifts the relative positions of the test masses and alters the interference pattern of the laser beams.

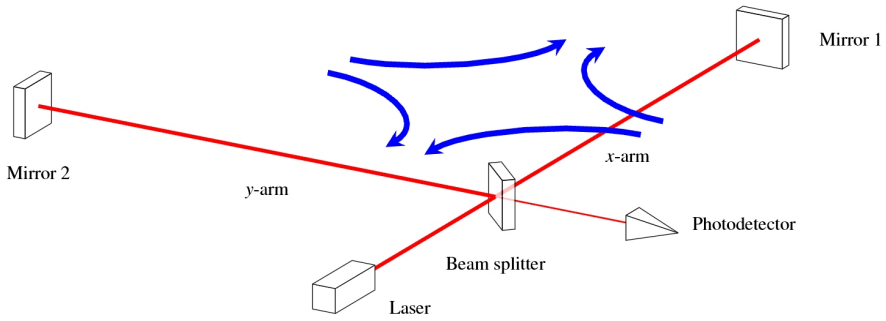

Figure 1.3: Idealised Michelson interferometer with laser, beam splitter, end mirrors, and photodetector at the exit port. The blue arrows represent a perpendicularly propagating, linearly polarised gravitational wave.

1.3.1 Advanced LIGO

The Advanced LIGO observatories operate two 4-km long laser interferometers located in Hanford, Washington, and Livingston, Louisiana [2]. Their seismic isolation systems include external active platforms called Hydraulic External Pre-Isolators (HEPI), and internal systems known as HAM-ISI and BSC-ISI, installed inside vacuum chambers. The core optics are suspended from quadruple pendulums, with the final test masses weighing around 40 kg. These suspensions contribute strong passive isolation to help reach the

design sensitivity of around $2 \cdot 10^{-23}/\sqrt{\text{Hz}}$ at 200 Hz.

Figures 1.4 and 1.5 show schematics and CAD representations of the isolation systems used in LIGO's BSC and HAM chambers, respectively. These images highlight the complexity and precision of the multi-stage platforms supporting both core and auxiliary optics.

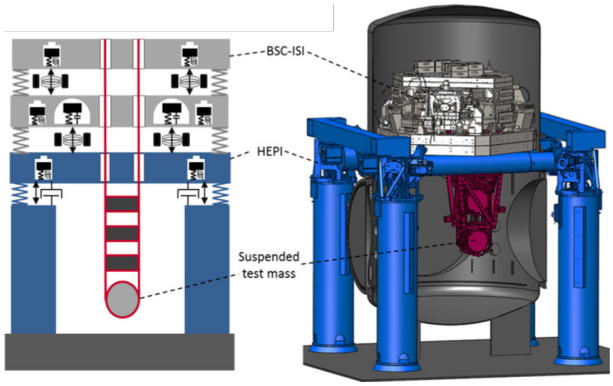

Figure 1.4: Schematic and CAD model of the isolation systems supporting the core optics in the BSC chambers [2].

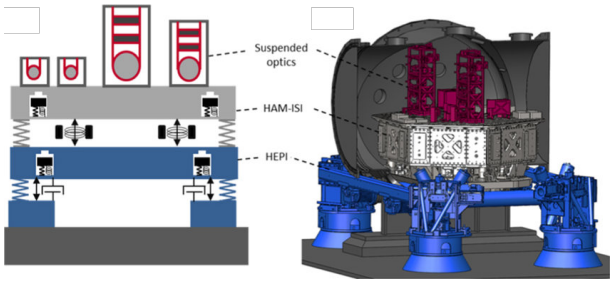

Figure 1.5: Schematic and CAD model of the isolation systems supporting the auxiliary optics in the HAM chambers [2].

1.3.2 Advanced Virgo

Located near Pisa, Italy, Advanced Virgo [3] uses the Super Attenuator system to achieve seismic isolation. As shown in Fig. 1.6, this system begins with an Inverted Pendulum (IP) that provides horizontal flexibility, followed by a vertical chain of mechanical filters and a marionette stage for angular control. The final test masses are monolithically suspended to reduce thermal noise and enhance alignment stability.

1.3.3 KAGRA

KAGRA [18] is a gravitational wave observatory located underground in the Kamioka mine in Japan. This unique location significantly reduces seismic and anthropogenic noise. KAGRA also implements cryogenic cooling of its test masses to lower thermal noise. Its

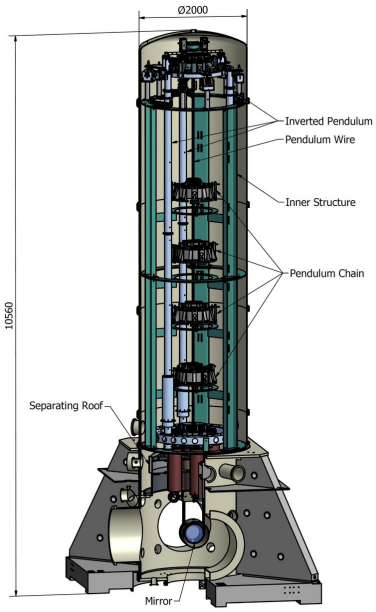

Figure 1.6: Schematic view of the Virgo Superattenuator [3].

seismic isolation system combines Inverted Pendulums and mechanical filters similar to Virgo, culminating in suspended sapphire mirrors cooled to around 20 K.

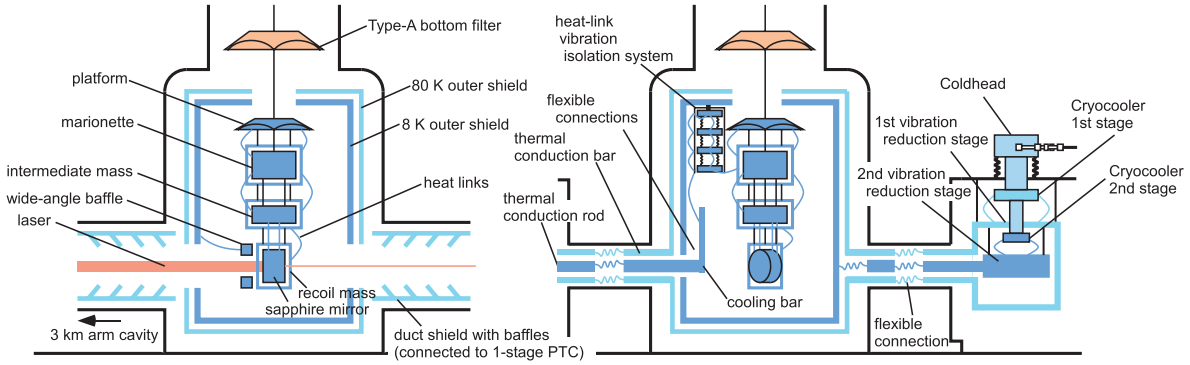

Figure 1.7: Schematic of the cooling system. Side view of the cryostat from the direction orthogonal to the arm (left) and another side view at an angle of 30° from the direction indicated in the left-hand panel (right) from [4].

1.3.4 GEO600

GEO600 [19], located near Hannover, Germany, is a smaller interferometer with 600-meter arms. Though not designed for large-scale detection, it has served as a testbed for innovations like squeezed-light injection and advanced suspension systems. The interferometer employs triple pendulum suspensions and passive isolation stacks to minimize ground vibrations.

1.3.5 Einstein Telescope

The Einstein Telescope [16] is a proposed third-generation observatory. Designed to be constructed underground, ET will benefit from reduced seismic and gravity-gradient noise. Its triangular layout, with 10-km arms forming three nested interferometers, is optimized for broad frequency coverage. Future figures, such as underground layout diagrams or triangular tunnel schematics, would help visualize this innovative concept.

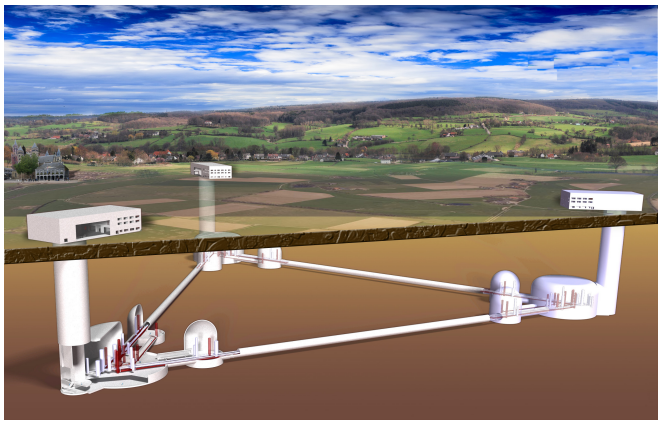

Figure 1.8: Drawing view of the Einstein Telescope (in development).

1.3.6 LISA

The Laser Interferometer Space Antenna (LISA) [5] will operate in space, free from seismic disturbances. Instead of suspensions, LISA uses drag-free control: test masses float freely inside spacecraft that adjust their position via micro-thrusters. Figure 1.9 illustrates the LISA constellation, with three spacecraft forming an equilateral triangle spanning 2.5 million kilometers. This configuration allows LISA to explore gravitational wave sources in the millihertz band.

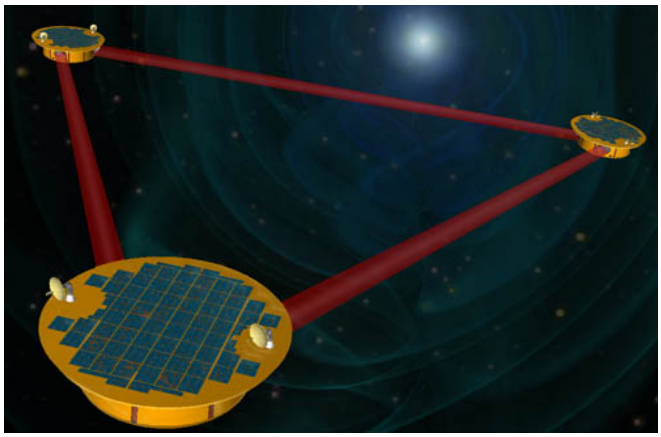

Figure 1.9: LISA constellation in space: the three satellites form a laser interferometer with 2.5 million km arms [5].

1.4 Specific problem

Designing suspension systems for gravitational wave detectors involves overcoming several parasitic effects that complicate control strategies. Among the most significant challenges are non-minimum phase zeros (NMPZ) and couplings between translational and rotational degrees of freedom.

Non-minimum phase behavior occurs when an input causes the system to initially respond in the opposite direction to its final steady-state output. Such counterintuitive dynamics often stem from unwanted couplings, such as translation inducing rotation and vice versa. As illustrated in Figure 1.10, these effects are particularly problematic for control system performance.

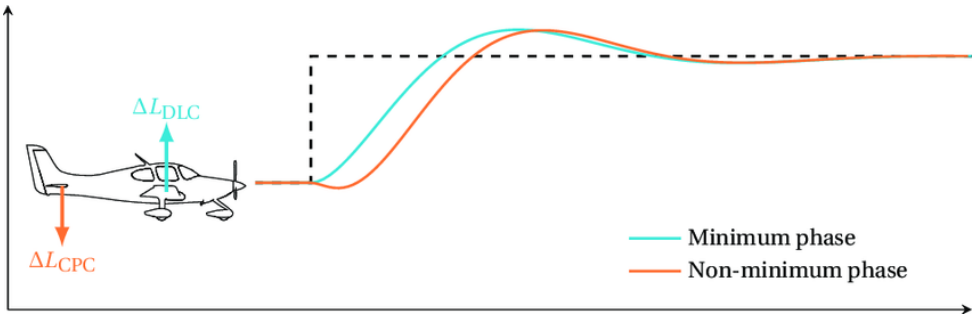

Figure 1.10: Qualitative comparison between a minimum phase and non-minimum phase altitude response.

These couplings introduce right-half-plane zeros into the system's transfer functions, which severely limit the achievable bandwidth and robustness of feedback controllers. Traditional strategies must therefore be adapted or redesigned to accommodate these fundamental limitations.

Controlling systems with non-minimum phase zeros is fundamentally more difficult than for minimum-phase systems. NMPZs cause an initial system response in the opposite direction of the intended motion, introducing phase lag and limiting disturbance rejection. In the time domain, this behavior is illustrated by Figure 1.10, where the NMP response shows an initial undershoot. This limits how quickly and aggressively a controller can act without risking instability.

This effect is not just theoretical, it appears in many real world scenarios. For example:

- In aircraft pitch control, sudden inputs can initially cause a reverse pitch movement.
- In outdated boiler systems, adjusting water temperature leads to unexpected overshoots before stabilization.

These examples highlight how NMP behavior restricts how aggressively one can apply corrections. In gravitational wave detectors, where control precision is crucial, such limitations must be addressed with care.

Advanced control techniques such as decoupling strategies, state observers, and robust control laws are required to address the presence of NMPZs. A key challenge lies in the fact that these zeros often arise from the coupling of horizontal translation with rotational motion, leading to phase inversion and potential instability when gain is increased near critical frequencies [20].

Inertial sensors such as geophones or capacitive accelerometers cannot distinguish between horizontal linear acceleration and tilt about a horizontal axis. Below the frequency of the NMPZ, tilt dominates the measurement; above it, the correct horizontal motion is captured. In platforms like HEPI and ISI, NMPZs often originate from internal bending modes, such as local flexing of the structure under actuator forces [21]. These dynamics constrain control bandwidth and thus limit seismic isolation performance especially in systems requiring extreme sensitivity.

To mitigate these effects, Advanced LIGO incorporated several mechanical and control design improvements [21]:

- Massive and stiff platform structures to suppress internal modes,
- Filter designs with reduced gain near NMPZ frequencies,
- Feedforward inertial control to reduce disturbances while avoiding unstable dynamics.

A key mechanical innovation was the use of blade springs and flexure rods. As shown in Figure 1.11, triangular blades mounted horizontally allow vertical compliance while maintaining high stiffness, minimizing tilt effects.

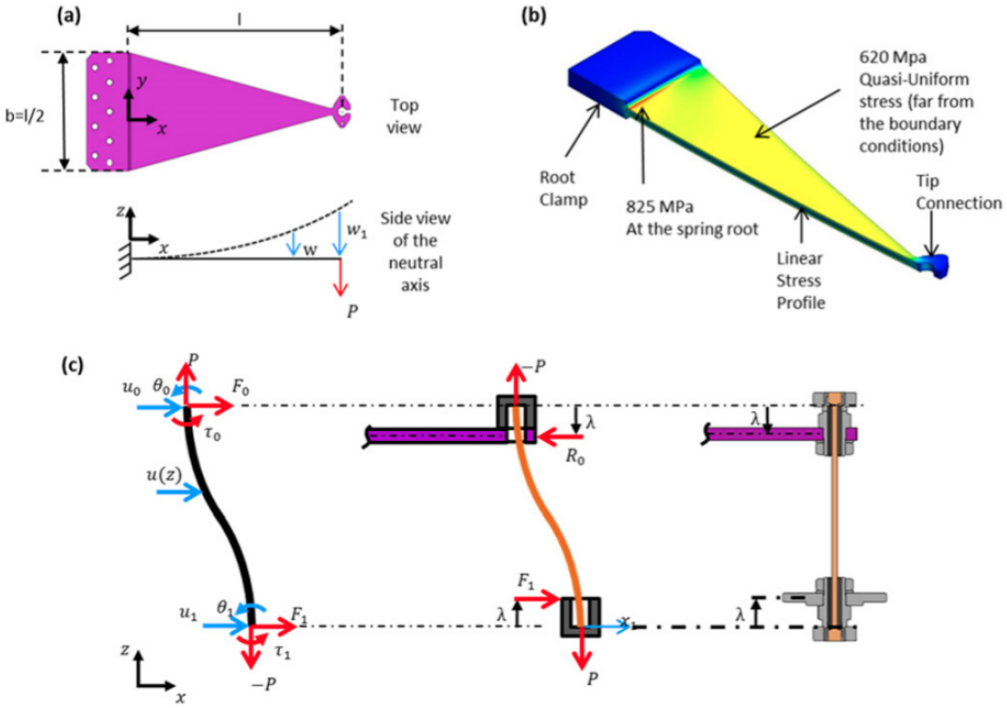

Figure 1.11: Blade springs and flexure rods used in seismic isolation platforms.

The flexure rods, designed around their zero-moment point, enable horizontal translation with minimal coupling to rotation. This mechanical decoupling aligns the system's six rigid-body modes with the Cartesian axes, improving seismic isolation and control precision. Figure 1.12 illustrates the two main types of isolation platforms: the BSC-ISI and HAM-ISI systems, showing both conceptual designs and physical implementations.

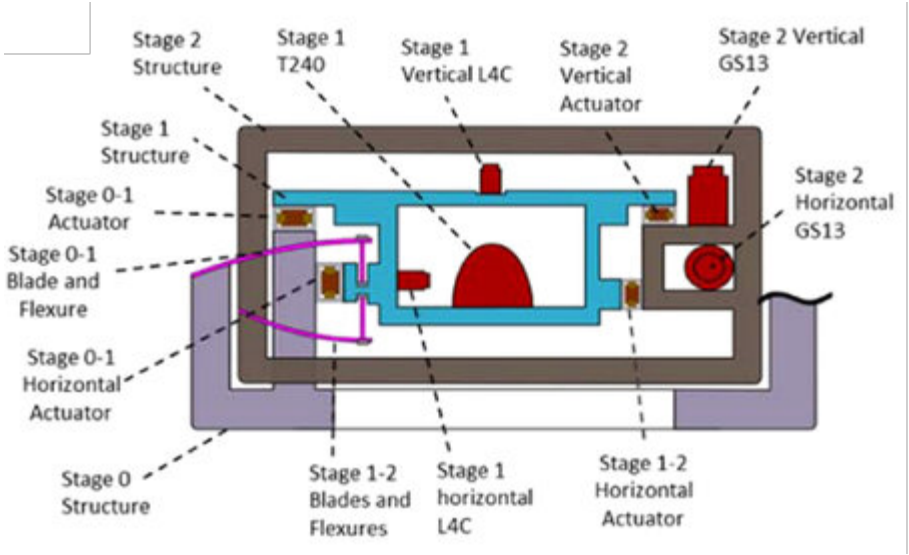

(a) Schematic representation of the BSC-ISI system

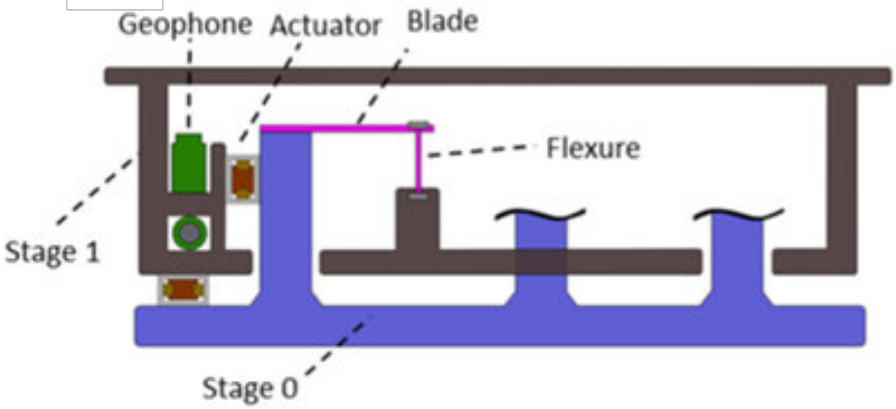

(b) Conceptual representation of the HAM-ISI

Figure 1.12: Schematic and CAD models of the BSC and HAM isolation platforms.

The next chapter will provide a more detailed frequency-domain analysis of these phenomena.

Chapter 2

Active isolation

Active isolation involves the use of actuators to counteract vibrations and enhance the dynamic behavior of a mechanical structure. This strategy can achieve levels of vibration attenuation that are unachievable by passive means alone. In many practical applications, active and passive systems are combined to exploit the robustness of passive components and the adaptability of active control.

In this chapter, the modeling framework is presented for active isolation platforms by drawing a parallel between a fully actuated six-degree-of-freedom system, such as the one shown in Figure 2.1, and a simplified rigid body model with a reduced number of degrees of freedom. This abstraction enables to study key properties of such systems particularly how their behavior is affected by the location of zeros in the transfer function.

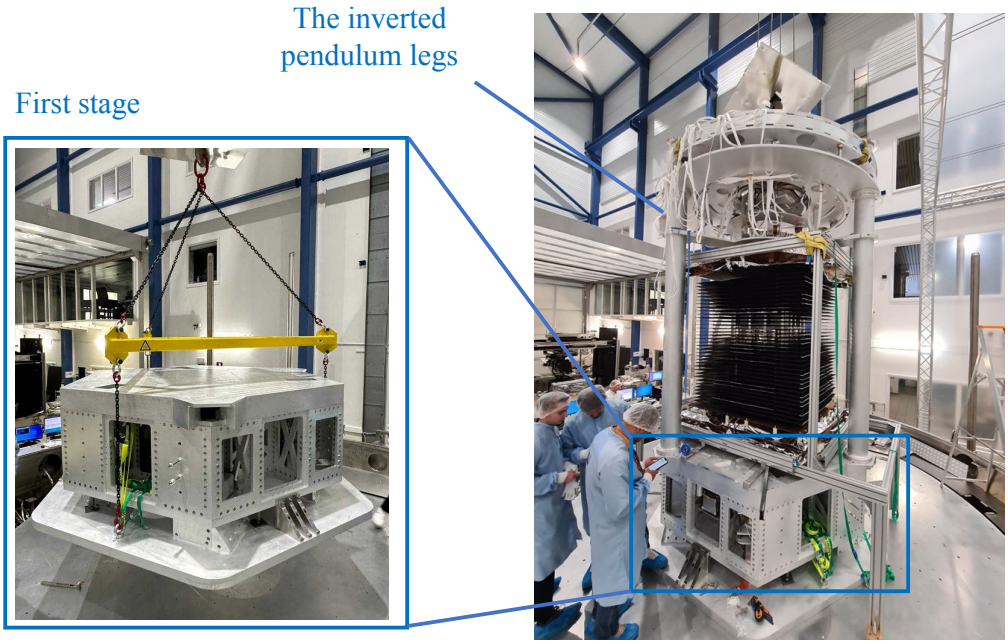

Figure 2.1: ETEST prototype view with the 6-DoF active platform.

Sections 2.3, 2.4, and 2.5 examine different configurations in increasing complexity, progressively highlighting how system structure, sensor placement, and actuation strategy can introduce or mitigate non-minimum phase behavior.

2.1 Principle of an inertial sensor

Inertial sensors (IS) are used to estimate the absolute motion of a structure by measuring relative displacements. Although commonly referred to as absolute motion sensors, they actually detect the relative displacement between an inertial reference mass and the structure to which the sensor is attached. As such, they only approximate absolute motion over a certain frequency range, which depends on the mechanical characteristics of the sensor.

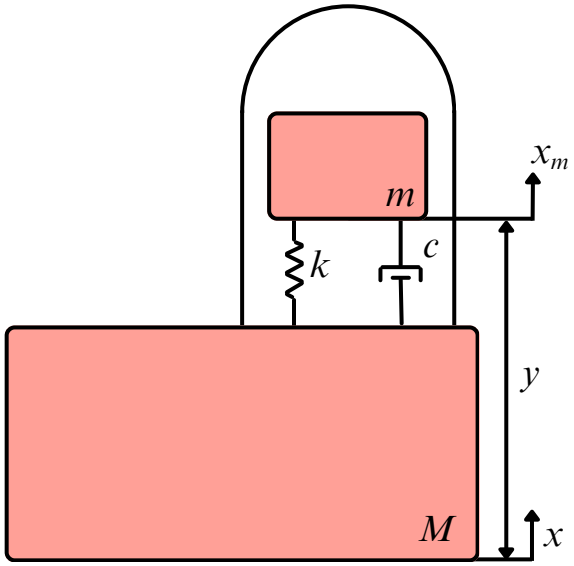

Figure 2.2: Schematic model of an inertial sensor. The measured signal y corresponds to the relative displacement between the inertial mass m and the supporting mass M.

The simplified model of the inertial sensor consists of a mass m suspended from a moving base using a spring-damper system with stiffness k and damping coefficient c. Let $x(t)$ denote the absolute displacement of the base, and $x_m(t)$ the absolute displacement of the inertial mass. The sensor measures the relative displacement

$$y(t) = x_m(t) - x(t). \tag{2.1}$$

The dynamic of the system is described by the equation

$$m\ddot{x}_m = -c(\dot{x}_m - \dot{x}) - k(x_m - x), \tag{2.2}$$

which can be rewritten in terms of the measured signal $y(t)$ as

$$m\ddot{y} + c\dot{y} + ky = -m\ddot{x}. \tag{2.3}$$

In the Laplace domain, the transfer function from the absolute motion of the base $X(s)$ to the sensor output $Y(s)$ is

$$T_{xy}(s) = \frac{Y(s)}{X(s)} = -\frac{ms^2}{ms^2 + cs + k}. \tag{2.4}$$

This transfer function exhibits two key behaviors depending on frequency:

- **High-frequency regime** (i.e., frequencies above the natural frequency $\omega_0 = \sqrt{k/m}$): The relative displacement $y(t)$ becomes quasi-equal ($\frac{Y(s)}{X(s)} \approx -1$) to the absolute displacement $x(t)$. In this range, the sensor behaves like an absolute displacement sensor.
- **Low-frequency regime**: The output is proportional to the base acceleration, scaled by the inertial mass m. In this case, the sensor functions effectively as an accelerometer.

Additional transfer functions relate the output to the base velocity and acceleration

$$T_{\dot{x}y}(s) = \frac{Y(s)}{\dot{X}(s)} = -\frac{ms}{ms^2 + cs + k}, \tag{2.5}$$

$$T_{\ddot{x}y}(s) = \frac{Y(s)}{\ddot{X}(s)} = -\frac{m}{ms^2 + cs + k}. \tag{2.6}$$

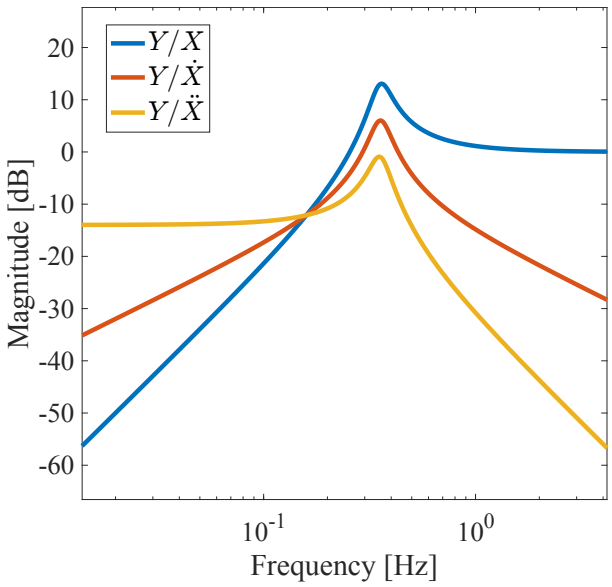

Figure 2.3: Various transmissibilities of the inertial sensor output. Parameters: $m = 10$ [kg], $k = 50$ [N/m], $c = 5$ [N·s/m].

These expressions illustrate that, depending on the frequency, the sensor output may serve as an accurate estimator of displacement, velocity, or acceleration. For applications requiring sensitivity at very low frequencies such as seismic isolation. While inertial sensors are powerful tools for measuring motion, their effective operation is limited to specific frequency ranges. Their design must carefully balance sensitivity, bandwidth, and mechanical robustness.

2.2 Modeling framework and methodology

This section describes the modeling and simulation strategy adopted to investigate the behavior of system zeros in the presence of inertial sensors.

The primary simulation environment is Simscape, a MATLAB extension that enables the construction of physics-based models incorporating mechanical constraints and gravitational effects. In parallel, analytical derivations are developed in selected cases to gain physical insight into the mechanisms behind the emergence and characteristics of non-minimum phase zeros. The methodology involves validating the Simscape model by comparing its transfer functions with those derived analytically. The reference model used throughout this study consists of two rigid cubic bodies with respective masses M and m. The system is grounded on a fixed, infinitely large rigid surface. A configurable joint connects the main mass M to the ground and may be set as purely translational, purely rotational, or a combination of both (e.g., a pin-slot joint). The configuration also includes parametric placement of springs, actuators, and sensors, allowing flexibility to explore various structural scenarios.

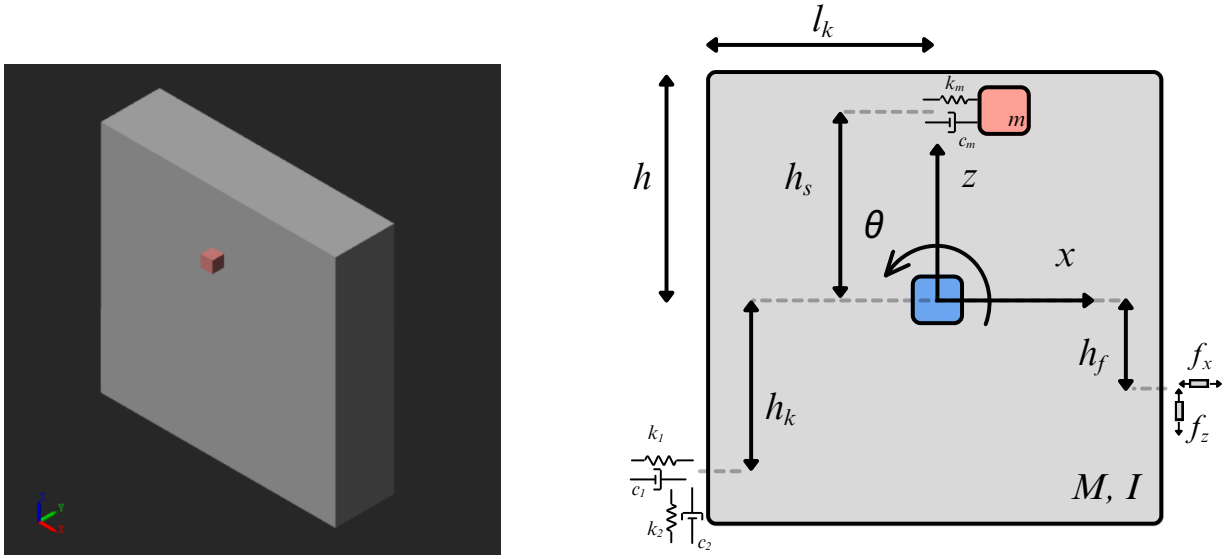

(a) Simscape implementation (b) Schematic representation

Figure 2.4: Reference model used for zero analysis in various configurations. The inertial sensor is represented in pink. The blue joint can be configured as translational, rotational, or combined, depending on the mechanical scenario under study.

Model parameters

Table 2.1 lists the fixed parameters used throughout the simulations, while Table 2.2 presents the configuration-dependent parameters that are varied in different scenarios and Table 2.3 shows the different measured states that will be used in following sections.

Symbol	Description	Value [unit]
g	Gravitational acceleration	9.80665 [m/s^2]
M	Mass of the platform	100 [kg]
m	Mass of the inertial sensor	1 [kg]
l_k	Half-width (spring position)	1 [m]
l_f	Half-width (actuator position)	1 [m]
h	Half-height of the platform	1 [m]
k_1	Horizontal spring stiffness	12,915 [N/m]
c_1	Horizontal damping coefficient	4 [N·s/m]
k_2	Vertical spring stiffness	1,000 [N/m]
c_2	Vertical damping coefficient	2 [N·s/m]
k_h	Sensor stiffness	2 [N/m]
c_h	Sensor damping coefficient	10^{-2} [N·s/m]
x_h	Sensor horizontal offset	0 [m]

Table 2.1: Fixed parameters used in the simulation model

Symbol	Description	Expression [unit]
h_f	Vertical position of actuator	$0.85\,h$ [m]
h_k	Vertical position of spring	$0.25\,h$ [m]
h_s	Vertical position of sensor	$-h$ [m]

Table 2.2: Variable parameters depending on the system configuration

Symbol	Description
θ	Rotation angle of the platform
x	Translation motion of the platform
y	Output of the inertial sensor
x_m	Absolute displacement of the IS
f_1	Applied horizontal force
f_2	Applied horizontal force

Table 2.3: Measured and defined quantities used in the analysis

Classification of zeros

To analyze the system dynamics, especially the impact of sensor and actuator placement, zeros are classified according to the sign and nature of their real parts. This classification will be used throughout the study to interpret the nature of the observed zeros in the system's transfer functions.

Category	Description
Minimum phase	All zeros have non-positive real part
Non-minimum phase (real)	One pair of zeros with positive real part
Non-minimum phase (complex)	One pair of complex-conjugate zeros with positive real parts
Two non-minimum phase zeros	Two distinct pairs of zeros with positive real parts

Table 2.4: Classification of system zeros

This classification provides a useful framework for interpreting the results of the parametric studies and understanding how mechanical configurations influence the control limitations imposed by non-minimum phase behavior.

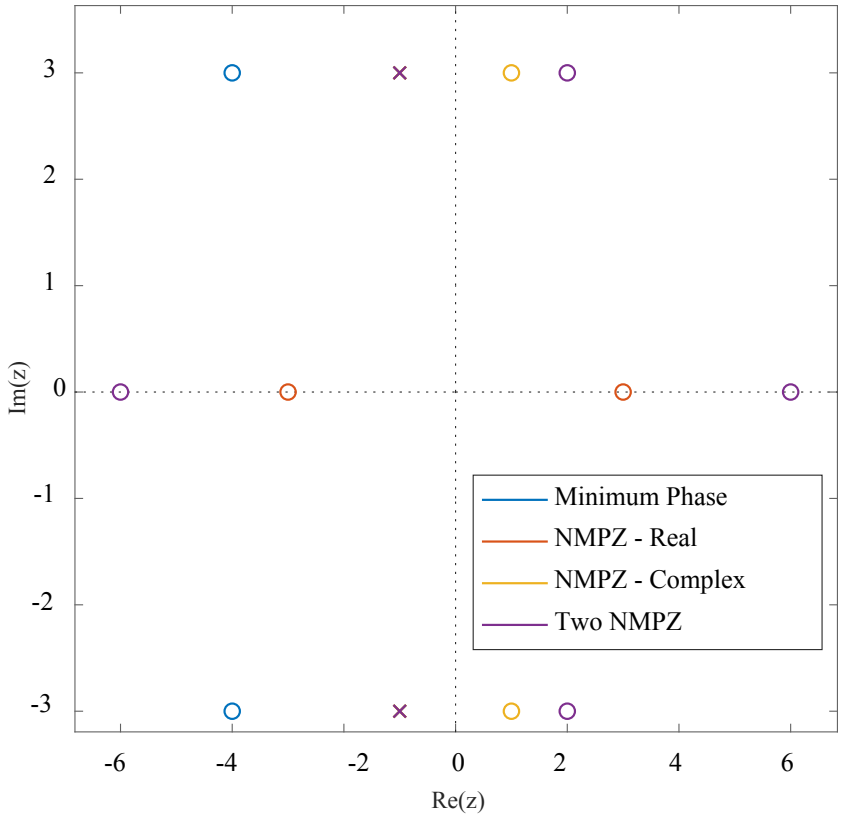

Figure 2.5: Classification of the different zeros in Imaginary-Real plane.

2.3 Model of a 1-DoF active platform

Active control strategies can be employed to enhance vibration isolation performance. Unlike passive systems, which rely solely on mechanical components, active isolation systems utilize actuators to apply corrective forces to the platform in response to measured motion. This allows for more effective suppression of vibrations, particularly at low frequencies.

Figure 2.6 shows a simplified one-degree-of-freedom model of such an active system. The platform is modeled as a mass M supported by a linear spring of stiffness k and a damper with damping coefficient c. An actuator exerts a control force f_1 on the platform. An horizontal inertial sensor measures motion, providing an estimate of the absolute displacement $x(t)$ of the platform.

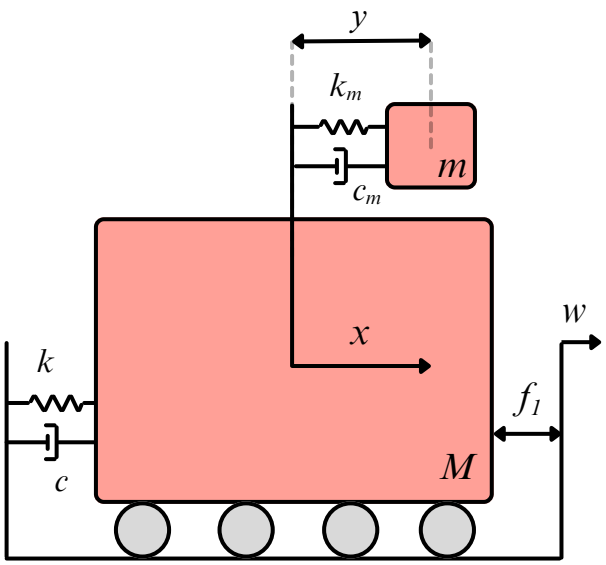

Figure 2.6: Simplified model of a 1-DoF active platform along the x-axis. The system consists of stiffness k, damping c, and an actuator that applies force f_1. Absolute displacement x is estimated using the inertial sensor output y.

2.3.1 Analytical model

The dynamics of a one-degree-of-freedom vibration isolation platform equipped with an inertial sensor can be described using a state-space representation. Let the state vector be defined as

$$x = \begin{bmatrix} x \\ y \\ \dot{x} \\ \dot{y} \end{bmatrix}, \tag{2.7}$$

where x is the absolute displacement of the platform, and y is the relative displacement of the inertial sensor mass.

The equations of motion are then written in the standard state-space form

$$\dot{x} = Ax + Bu, \quad y = Cx + Du, \tag{2.8}$$

with the state-space matrices given by

$$A = \begin{bmatrix} 0 & 0 & 1 & 0 \\ 0 & 0 & 0 & 1 \\ -\frac{k_1}{M} & \frac{k_m}{M} & -\frac{c_1}{M} & \frac{c_m}{M} \\ \frac{k_1}{M} & -\left(\frac{k_m}{M}+\frac{k_m}{m}\right) & \frac{c_1}{M} & -\left(\frac{c_m}{M}+\frac{c_m}{m}\right) \end{bmatrix}, \quad B = \frac{1}{M}\begin{bmatrix} 0 & 0 \\ 0 & 0 \\ 1 & 1 \\ -1 & -1 \end{bmatrix}. \tag{2.9}$$

The input vector $u = \begin{bmatrix} f_1 & w \end{bmatrix}^T$ includes both the control force and the ground displacement. The output vector $y = \begin{bmatrix} x & y \end{bmatrix}^T$ corresponds respectively to the absolute and relative displacements of the platform and the sensor mass. This formulation enables straightforward analysis of the system's response to both ground disturbances and active control inputs, as well as the development of feedback control strategies that account for the coupled dynamics between the platform and the sensor.

To mitigate the effects of ground disturbances on the platform, an active control scheme is implemented. The actuator generates a control force f_1, which is determined based on the motion measured by an inertial sensor. This sensor provides an estimate of the absolute displacement x of the platform, from which the control signal is derived.

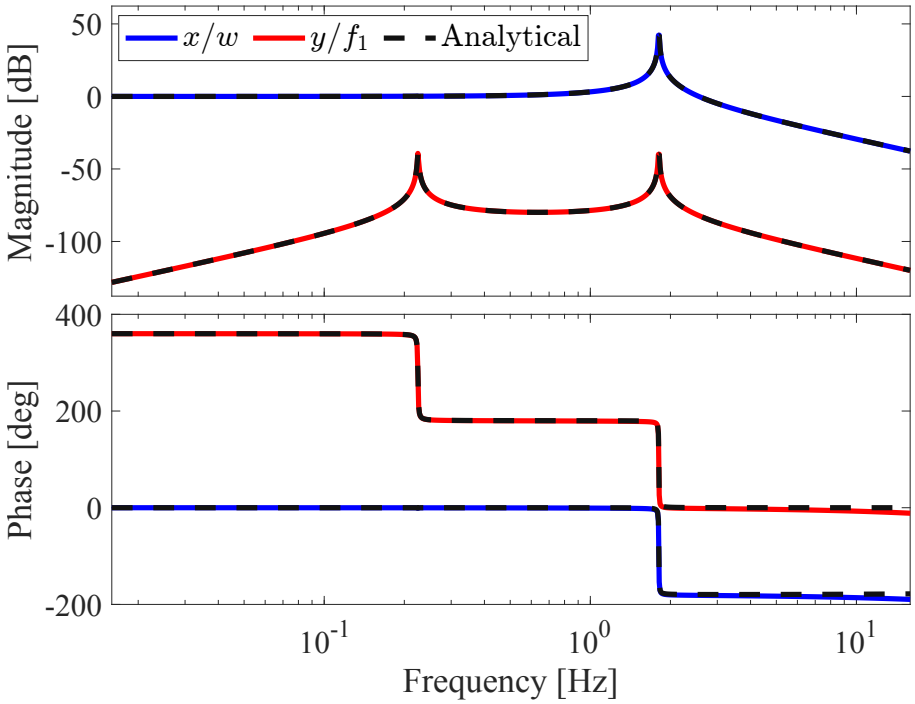

Figure 2.7: Transfer function of a 1-DoF active platform with inertial sensor feedback. This figure is obtained with a linearized simscape model.

It can be seen in Figure 2.7 that the transfer function used for control is relatively simple and exhibits a zero located at or near 0 Hz. This characteristic is particularly advantageous for feedback control design. A zero at the origin implies that the system has an inherent differentiating behavior, which introduces a phase lead at low frequencies.

As a result, it does not impose destabilizing phase lag within the typical control bandwidth, unlike non-minimum phase zeros located in the right-half of the complex plane. Moreover, the presence of a low-frequency or DC zero means that standard compensators such as proportional-integral (PI) or lead controllers can be effectively designed without needing to account for adverse phase behavior. The control loop can tolerate higher gain at low frequencies, allowing better disturbance rejection and reference tracking. In practice, this leads to faster convergence, simpler tuning rules, and greater robustness margins.

2.4 Effect of tilt-horizontal coupling

In this section, a simplified model of a rigid pendulum is used to illustrate how the placement of the inertial sensor affects the coupling between tilt and horizontal translation. The pendulum is equipped with horizontal and vertical springs, both damped. Two configurations are considered: one with the sensor placed at the **top** of the pendulum, and the other with it placed at the **bottom**. The objective is not to perform an exhaustive analytical derivation, but rather to highlight a fundamental behavior related to the **sensor's vertical position relative to the center of rotation**.

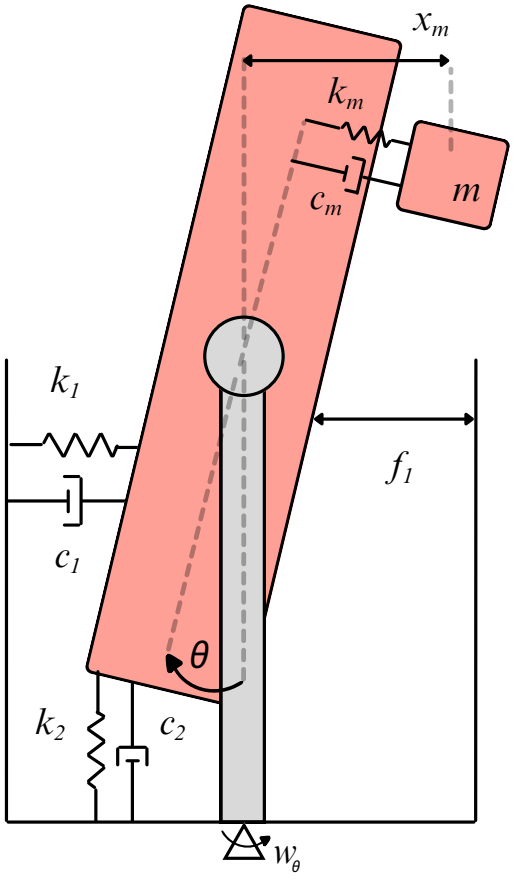

Figure 2.8: Conceptual model of a pendulum (or an IP) where the inertial sensor can be placed at the top and then at the bottom.

2.4.1 Analytical model

Assuming that the sensor rotates with the structure, defining the measured displacement as the combination of translation and rotation

$$x_m(t) = y(t) + R \cdot \theta(t) \tag{2.10}$$

Starting from the coupled system of equations and write the differential equations as

$$I\ddot{\theta} = h_f f_1 - c_\theta \dot{\theta} - k_\theta \theta + mgR\theta - (mgy - k_h R y - c_h R \dot{y}) \tag{2.11}$$

$$m(R\ddot{\theta} + \ddot{y}) = mg\theta - c_h \dot{y} - k_h y \tag{2.12}$$

Note that for simplicity, stifness and damping have been converted into rotational but the expressions remain the same and defined as

$$c_\theta = c_1 h_k^2 + c_2 l_k^2, \tag{2.13}$$

$$k_\theta = k_1 h_k^2 + k_2 l_k^2. \tag{2.14}$$

Taking the Laplace transform gives

$$\begin{bmatrix} Is^2 + c_\theta s + k_\theta - mgR & mg - R(k_h + c_h s) \\ mRs^2 - mg & ms^2 + k_h + c_h s \end{bmatrix} \begin{bmatrix} \Theta \\ Y \end{bmatrix} = \begin{bmatrix} h_f F \\ 0 \end{bmatrix} \tag{2.15}$$

Assuming that the inertial sensor exerts negligible influence on the platform's rotational dynamics, its contribution in the first equation is removed,

$$\begin{bmatrix} Is^2 + c_\theta s + k_\theta - mgR & 0 \\ mRs^2 - mg & ms^2 + k_h + c_h s \end{bmatrix} \begin{bmatrix} \Theta \\ Y \end{bmatrix} = \begin{bmatrix} h_f F \\ 0 \end{bmatrix} \tag{2.16}$$

which defines the transfer function

$$\Theta(s) = T(s) \cdot F(s), \tag{2.17}$$

with

$$T(s) = \frac{h_f}{Is^2 + c_\theta s + k_\theta - mgR}. \tag{2.18}$$

Taking the second differential equation from 2.16 to compute the displacement of the inertial sensor, including the coupling with the platform's rotation

$$\left(ms^2 + c_h s + k_h\right) Y(s) = \left(mg - mRs^2\right) \Theta(s). \tag{2.19}$$

Solving for $Y(s)$ gives

$$Y(s) = \frac{m(g - Rs^2)}{ms^2 + c_h s + k_h} \cdot \Theta(s). \tag{2.20}$$

Substituting the previously derived expression $\Theta(s) = T(s) \cdot F(s)$, gives

$$Y(s) = \left(\frac{m(g - Rs^2)}{ms^2 + c_h s + k_h} \right) \cdot T(s) \cdot F(s). \tag{2.21}$$

Which can be rewritten as

$$\frac{Y(s)}{F(s)} = T(s) \cdot \frac{s^2 + g/R}{s^2 + 2\xi s + \omega_0}. \tag{2.22}$$

The numerator contains a zero at

$$s = \pm\sqrt{\frac{g}{R}}. \tag{2.23}$$

This system illustrates the phenomenon of *tilt-horizontal coupling*, where a sensor intended to measure horizontal acceleration also reacts to slow rotations in the gravitational field. This effect becomes particularly significant at **low frequencies**, where the gravitational component dominates the inertial measurement.

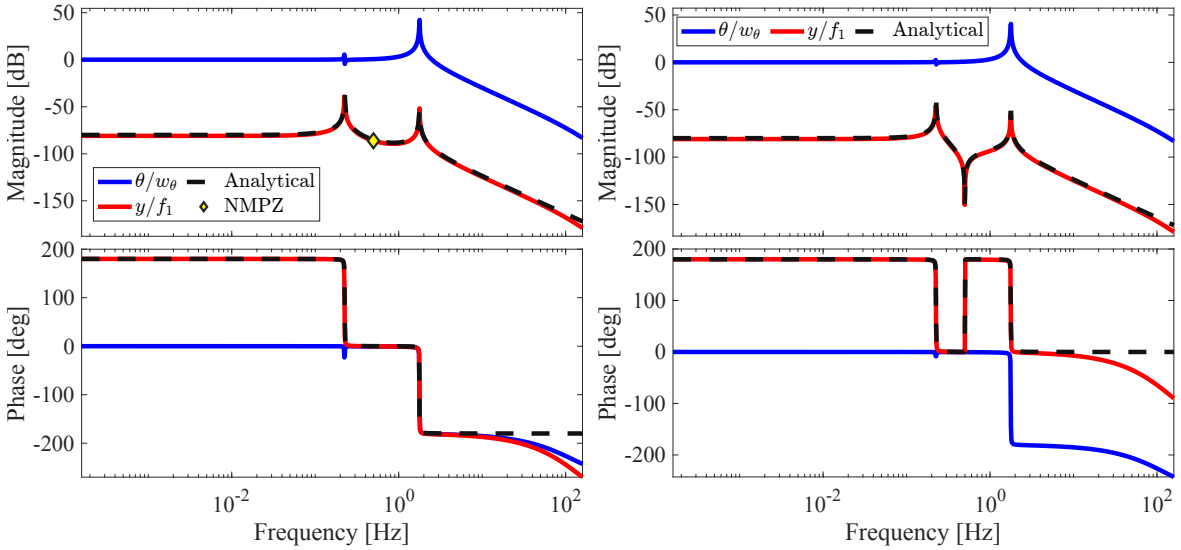

(a) Sensor placed above the center of rotation. (b) Sensor placed below the center of rotation.

Figure 2.9: Transfer function of a 1-DoF pendulum using an inertial sensor for feedback. These figures are obtained with the linearized simscape model introduced in Section 2.2 with a revolute joint.

This shows how the measured motion of the inertial sensor depends on both its own dynamics and the rotational behavior of the platform.

- If $R < 0$, the zeros are **imaginary** and the system is **minimum-phase**.
- If $R > 0$, the zeros are **real**, with one in the right-half plane: the system is **non-minimum phase**.

This non-minimum phase zero imposes destabilizing phase lag at low frequencies, degrading closed-loop performance and limiting disturbance rejection. Systems with non-minimum phase zeros impose fundamental trade-offs between performance and stability,

often requiring phase-limited designs and restricted control bandwidth. This analysis shows that the simple **positioning of the sensor** within the structure (above or below the rotation center) effectively changes the apparent **radius of curvature** R of its motion path, directly impacting the nature of the system's zero.

2.5 Model of a 2-DoF active platform

Considering the same mechanical system but this time with two degrees of freedom. The simplified model under consideration is illustrated below.

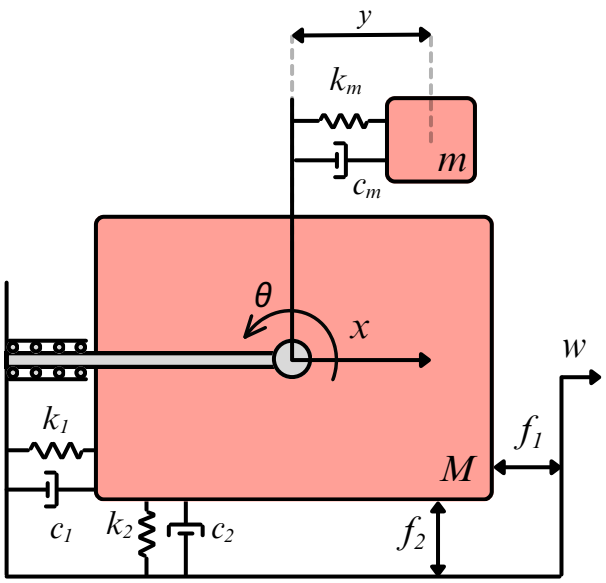

Figure 2.10: Simplified model of a 2-DOF active platform: horizontal translation x and rotation about the y-axis. The system includes two springs (k_1, k_2), two dampers (c_1, c_2), two actuators (f_1, f_2), and an inertial sensor located at h_s measuring relative displacement y.

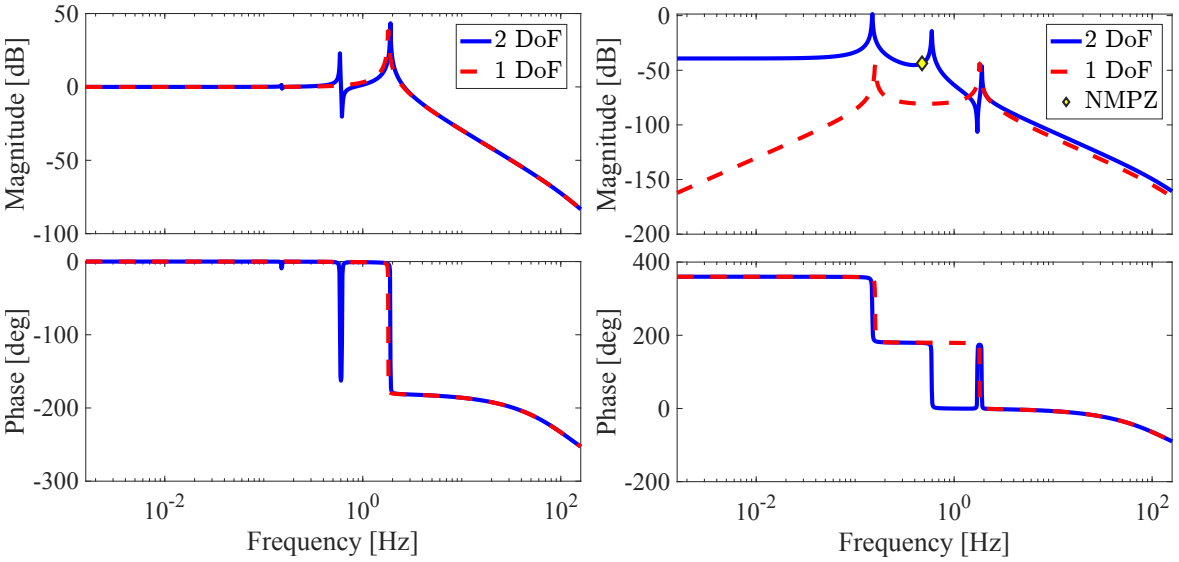

(a) Transfer function x/w (b) Transfer function y/f_1

Figure 2.11: Transfer function of a 2-DoF (blue) in translation along x and in rotation in the plane xz using an inertial sensor for feedback. The curves are obtained with the linearized Simscape model introduced in Section 2.2 with a pin-slot joint. The dash curves (red) comes from the 1-DoF system presented in Section 2.3.

Analysis of the transfer function between the input f_1 and the output y reveals the existence of two zeros, at least one of which is non-minimum phase depending on the system configuration. In order to understand the origin of each zero, it could be interesting to superimpose the curve of transfer function y/f_1 with the result obtained in the pendulum section.

2.5.1 Non-minimum phase zeros exploration

By superimposing the transfer function of a simple pendulum, it can be seen that one of the zeros in the 2-DoF system corresponds to the well-known tilt-horizontal coupling zero, which follows the classical behavior.

- The zero becomes non-minimum phase if the sensor is located above the rotation center,
- The zero is minimum phase if the sensor is placed below it.

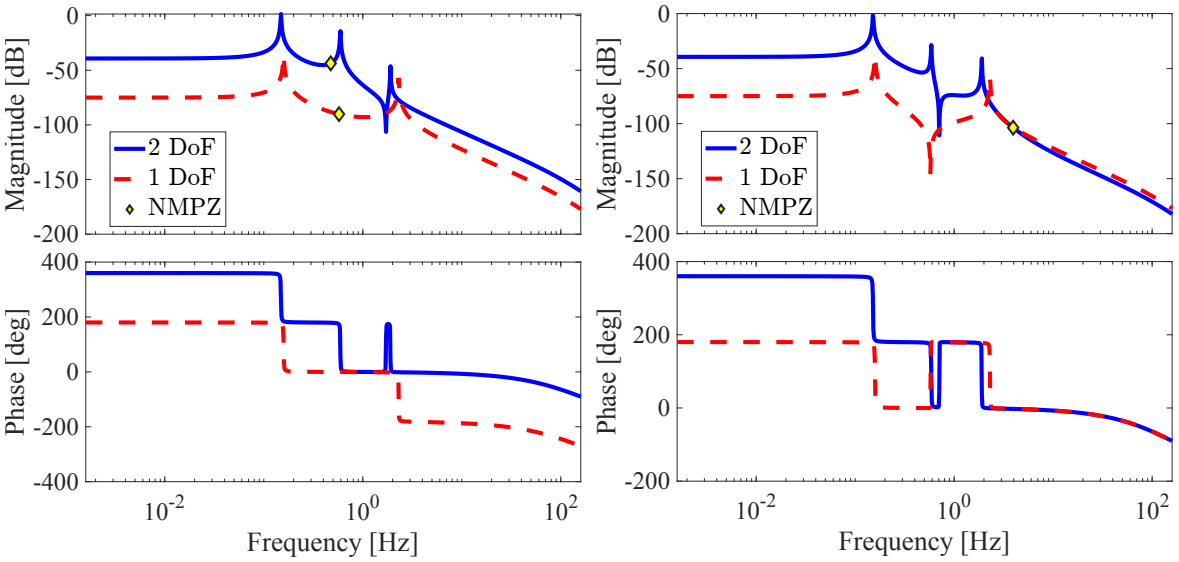

(a) Sensor placed above the center of rotation (b) Sensor placed below the center of rotation

Figure 2.12: Transfer function y/f_1 of a 2-DoF (blue) in translation along x and in rotation in the plane xz using an inertial sensor for feedback. The curves are obtained with the linearized Simscape model introduced in Section 2.2 with a pin-slot joint. The dash curves (red) comes from the 1-DoF system presented in Section 2.4.

However, the nature of the second zero changes with the configuration. By varying key parameters such as the vertical positions of the sensor, springs, and actuators, the system consistently retains at least one non-minimum phase zero. This strongly suggests that a second structural phenomenon is responsible for the emergence of this zero. But to be sure of that it requires to make varying more the parameters.

2.5.2 Parametric study

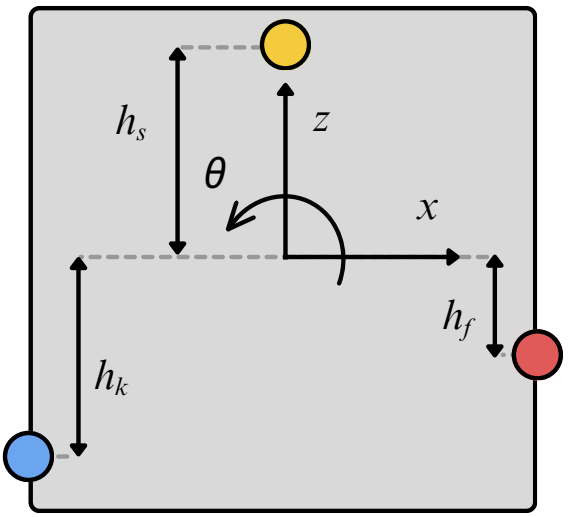

Figure 2.13: Schematic representation of the 2-DoF model in Section 2.2 by keeping only locations of the sensor, actuator, and spring.

To investigate this behavior, a parametric analysis is performed by varying the three key parameters for remembering:

- h_k: vertical position of the center of stiffness,
- h_f: vertical position of the actuator,
- h_s: vertical position of the sensor.

The following figures are generated with the same Simscape model, by varying the parameters and classify the zeros as presented in Table 2.4.

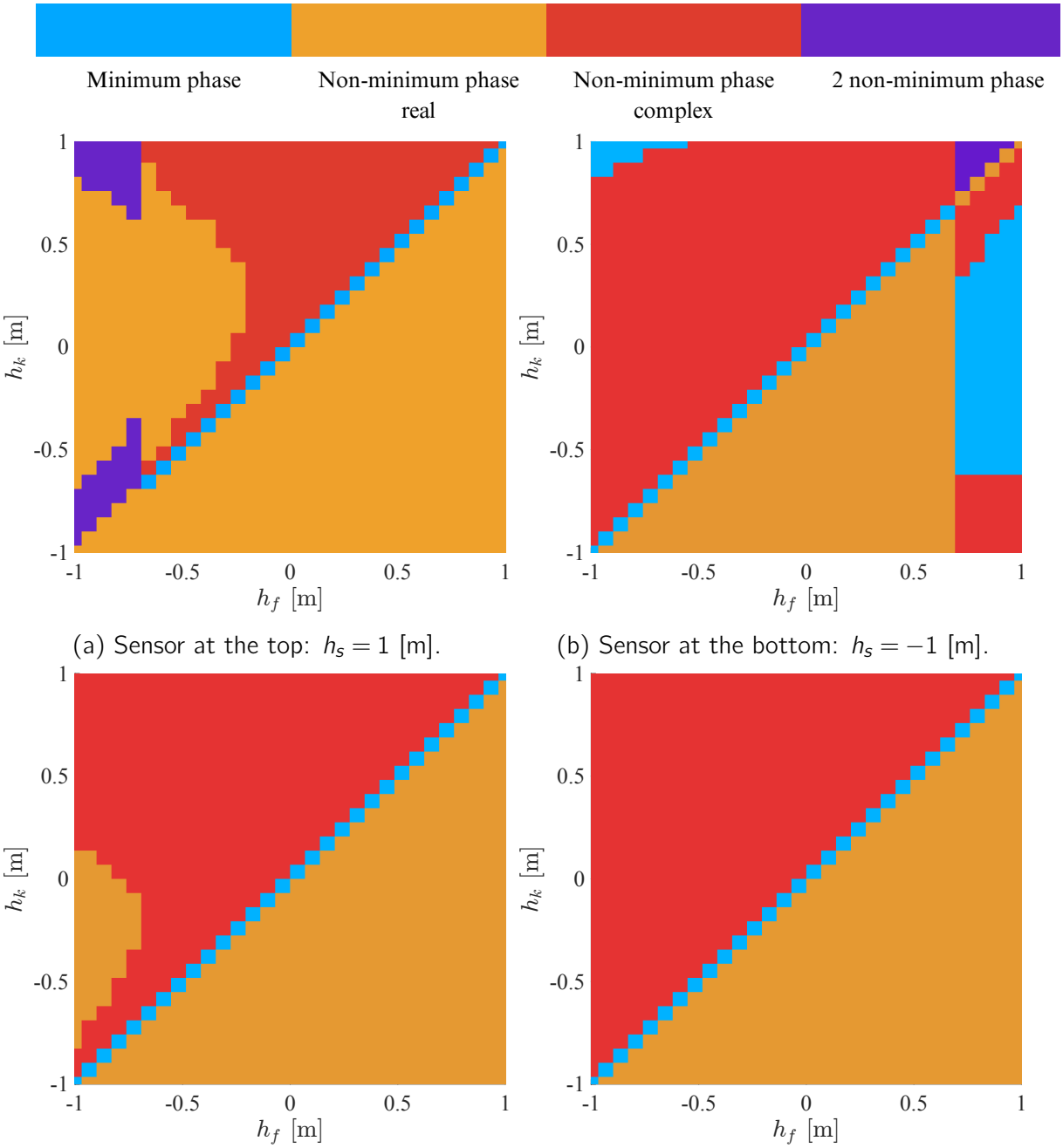

(a) Sensor at the top: $h_s = 1$ [m].

(b) Sensor at the bottom: $h_s = -1$ [m].

(c) Sensor above center: $h_s = 0.5$ [m].

(d) Sensor below center: $h_s = -0.5$ [m].

Figure 2.14: Nature of zeros for various sensor locations h_s and system configurations of the model from Section 2.2.

This analysis confirms that the majority of configurations result in the appearance of a non-minimum phase zero, reinforcing the idea that while one zero originates from tilt coupling, the second is linked to a distinct 2-DoF structural behavior.

2.5.3 Analytical derivation

To gain further insight let's take a closer look at the analytical expressions for the transfer functions corresponding to the model at Figure 2.10. Considering only one actuator f_1 as

input and ignoring the ground reaction and f_2, the Cramer's rule can be used to extract the transfer function of interest, specifically Y/F

$$(M+m)\ddot{x} = -f_1 - (x - h_k\theta)k_1 - (\dot{x} - h_k\dot{\theta})c_1 - k_h y - c_h\dot{y} \tag{2.24}$$

$$\begin{aligned}(I + mh_s^2)\ddot{\theta} = f_1 h_f + (x - h_k\theta)k_1 h_k + (\dot{x} - h_k\dot{\theta})c_1 z_s \\ -k_2\frac{l^2}{4}\theta - c_2\frac{l^2}{4}\dot{\theta} + c_h\dot{y}h_s + k_h y h_s - mgy\end{aligned} \tag{2.25}$$

$$m(\ddot{x} - h_s\ddot{\theta} + \ddot{y}) = -mg\theta - k_h y - c_h\dot{y} \tag{2.26}$$

Which gives in Laplaces domain

$$MKC \cdot \begin{bmatrix} X(s)/F_x(s) \\ \Theta(s)/F_x(s) \\ Y(s)/F_x(s) \end{bmatrix} = \begin{bmatrix} -1 \\ h_f \\ 0 \end{bmatrix} \tag{2.27}$$

with that matrix MKC correponds to

$$\begin{bmatrix} (M+m)s^2 + k_1 + c_1 s & -h_k k_1 - h_k c_1 s & k_h + c_h s \\ -k_1 h_k - c_1 h_k s & (I + mh_s^2)s^2 + (k_1 + c_1 s)h_k^2 + (k_2 + c_2 s)l_k^2 & -k_h h_s - c_h h_s s + mg \\ ms^2 & -mh_s s^2 + mg & ms^2 + k_h + c_h s \end{bmatrix} \tag{2.28}$$

The numerator of the transfer function $H_{fx\to sensor_x}(s)$ comes from

$$\text{num}(H_{f_1\to y})(s) = det(MKC_Y) =$$

$$\begin{vmatrix} (M+m)s^2 + k_1 + c_1 s & -h_k k_1 - h_k c_1 s & -1 \\ -k_1 h_k - c_1 h_k s & (I + mh_s^2)s^2 + (k_1 + c_1 s)h_k^2 + (k_2 + c_2 s)l_k^2 & h_f \\ ms^2 & -mh_s s^2 + mg & 0 \end{vmatrix} \tag{2.29}$$

$$\begin{aligned}\text{num}(H_{f_1\to y})(s) = \left((m+m_h)z_p \cdot z_f + I + m_h z_p^2\right)s^4 + \left(c_1(z_s - z_p)(z_s - z_f) + \frac{c_2 l^2}{4}\right)s^3 \\ + \left(-(m+m_h)g \cdot z_f + k_1(z_s - z_f)(z_s - z_p) + \frac{k_2 l^2}{4}\right)s^2 + (z_s - z_f)(c_1 s + k_1)g\end{aligned} \tag{2.30}$$

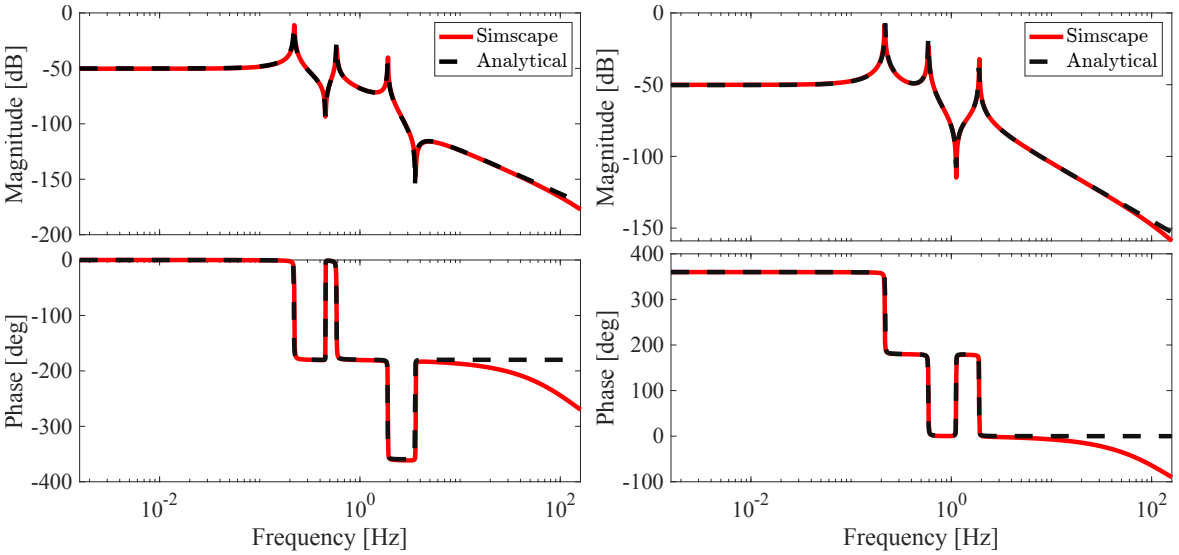

(a) Sensor placed above the center of rotation (b) Sensor placed below the center of rotation

Figure 2.15: Comparison between transfer function y/f_1 of the 2-DoF at Figure 2.10 obtained by either Simscape or analytically.

The expression is double checked but while insightful, it remains too complex to provide clear intuition about the system's zeros.

2.5.4 Analysis with perfect sensor

To isolate the effect of sensor dynamics, the inertial sensor is temporarily suppressed and only the position $p(x, z)$, where normally the inertial sensor is fixed, is used as measured state. This is done with an ideal sensor and the parametric study is repeated by keeping y as state but this time as the absolute displacement of the point $p(x, z)$. The zero distribution remains remarkably similar by looking between Figures 2.14 and 2.16, indicating that the second zero is not caused by sensor dynamics.

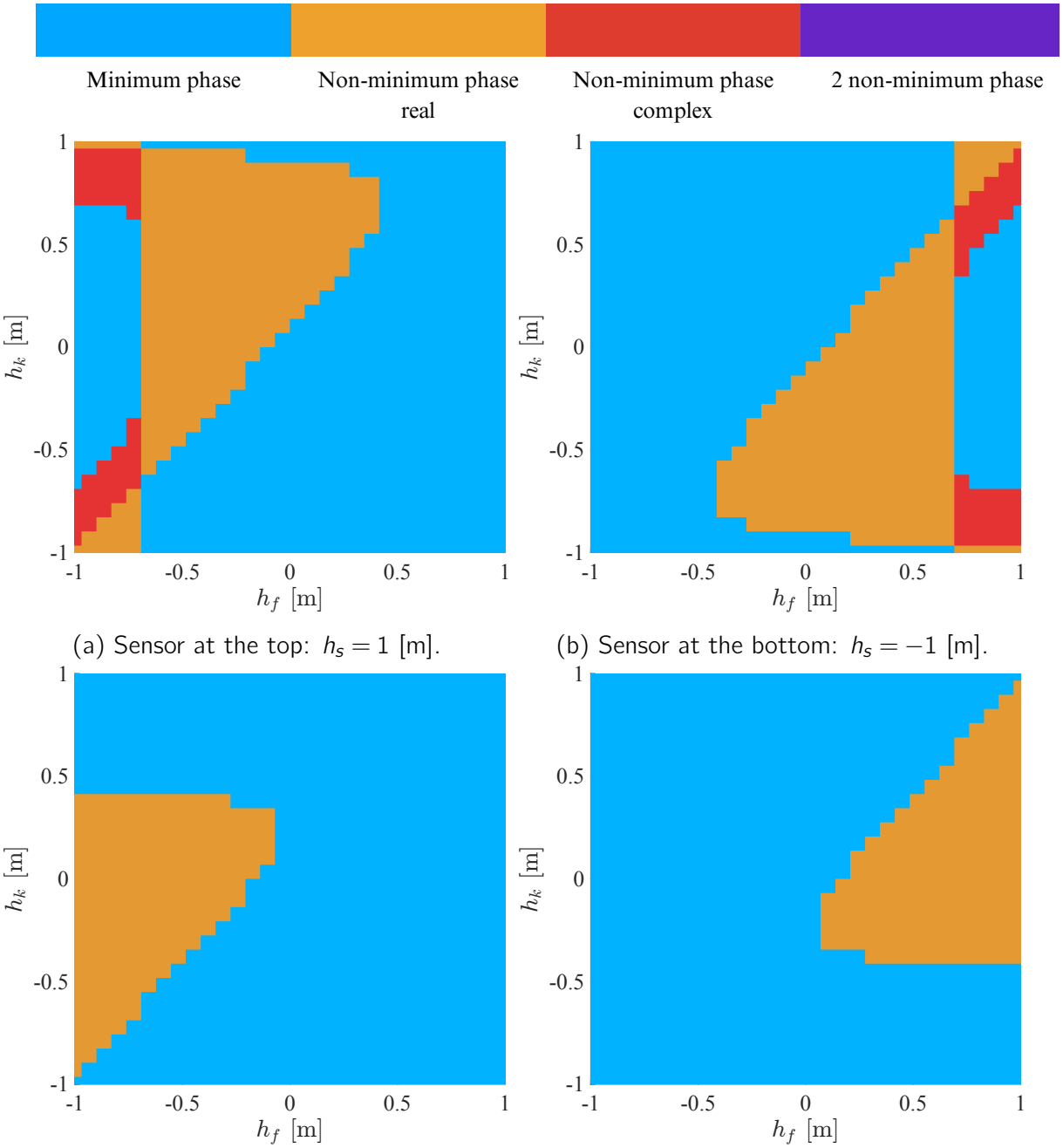

(a) Sensor at the top: $h_s = 1$ [m].

(b) Sensor at the bottom: $h_s = -1$ [m].

(c) Sensor above center: $h_s = 0.5$ [m].

(d) Sensor below center: $h_s = -0.5$ [m].

Figure 2.16: Nature of zeros for various sensor locations h_s and system configurations of the model from Section 2.2 but without IS.

The numerator of the simplified transfer function without inertial sensor and gravity neglected becomes

$$num(H_{f_1 \to y})(s) = (I + m h_s h_f)s^2 + (c_1(h_k - h_f)(h_k - h_s) + c_2 l_k^2)s + k_1(h_k - h_f)(h_k - h_s) + k_2 l_k^2 \quad (2.31)$$

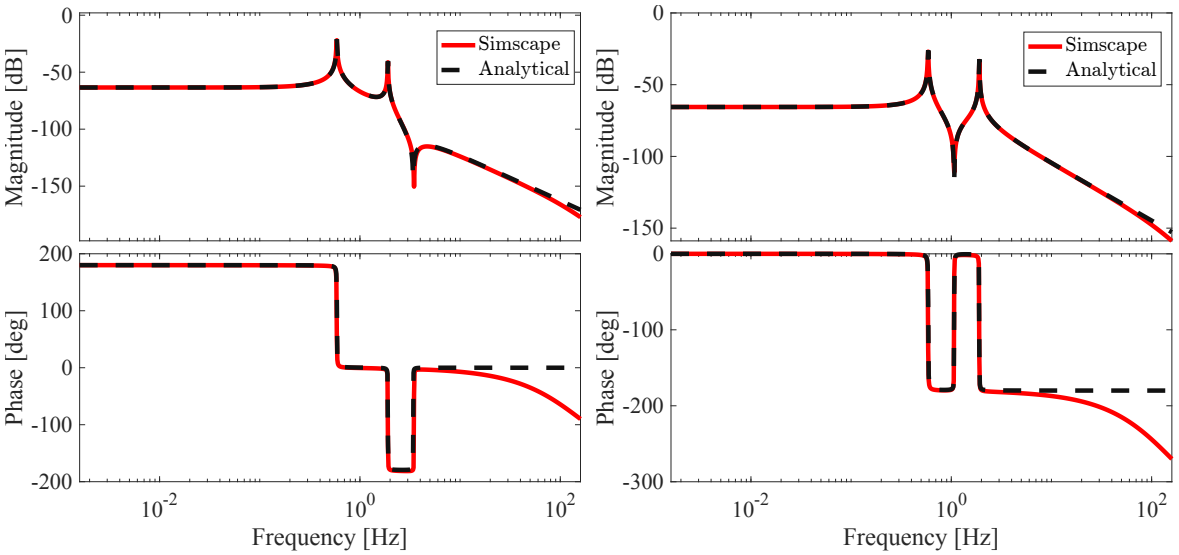

(a) Sensor placed above the center of rotation (b) Sensor placed below the center of rotation

Figure 2.17: Comparison between transfer function y/f_1 of the 2-DoF at Figure 2.10 without inertial sensor obtained by either Simscape or analytically.

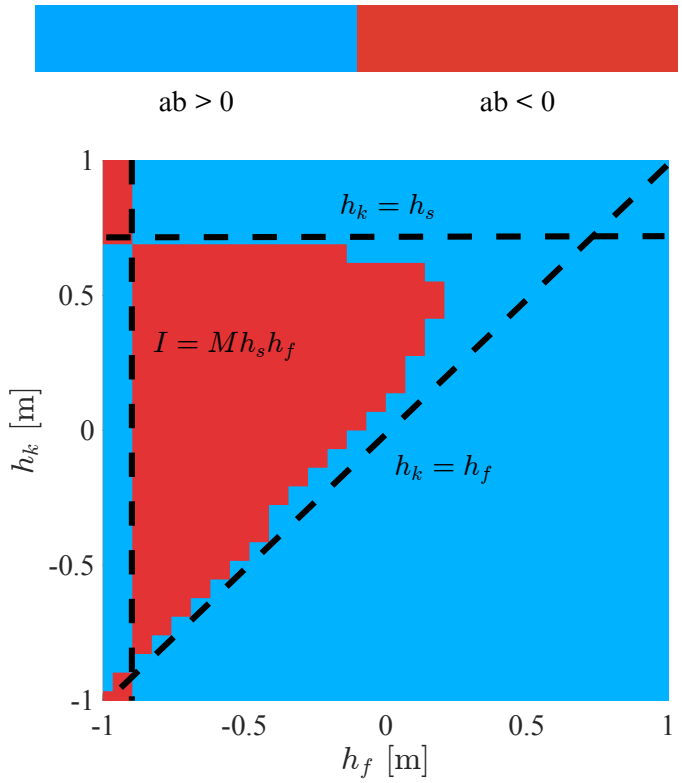

Figure 2.18: Region classification of the real part of the zeros, based on the value of ab for the 2-Dof without inertial sensor.

By neglecting k_2 and c_2 and considering that s are only for low frequencies, so $c_1 s <<$

k_1, the expression can be simplified as

$$num(H_{f_1 \to y})(s) = b \cdot s^2 + \frac{k_1}{a}, \tag{2.32}$$

where

$$ab = \frac{I + M h_s h_f}{(h_k - h_f)(h_k - h_s)}. \tag{2.33}$$

This expression provides a means to predict whether the zero is minimum or non-minimum phase. The term ab encodes both the mechanical decoupling between the actuator and CoK, and the sensor's vertical position relative to the CoK. The denominator of the Equation 2.33 determines the regions marked by the lines $h_k = h_s$ and $h_k = h_f$ and the numerator fixes the limit with the vertical line on the Figure 2.18.

2.5.5 Come back to the 2-DoF model with IS

To validate the analytical prediction from Equation 2.32, the relative error between the actual zero frequencies from the 2-DoF with inertial sensor and the predicted frequency is computed.

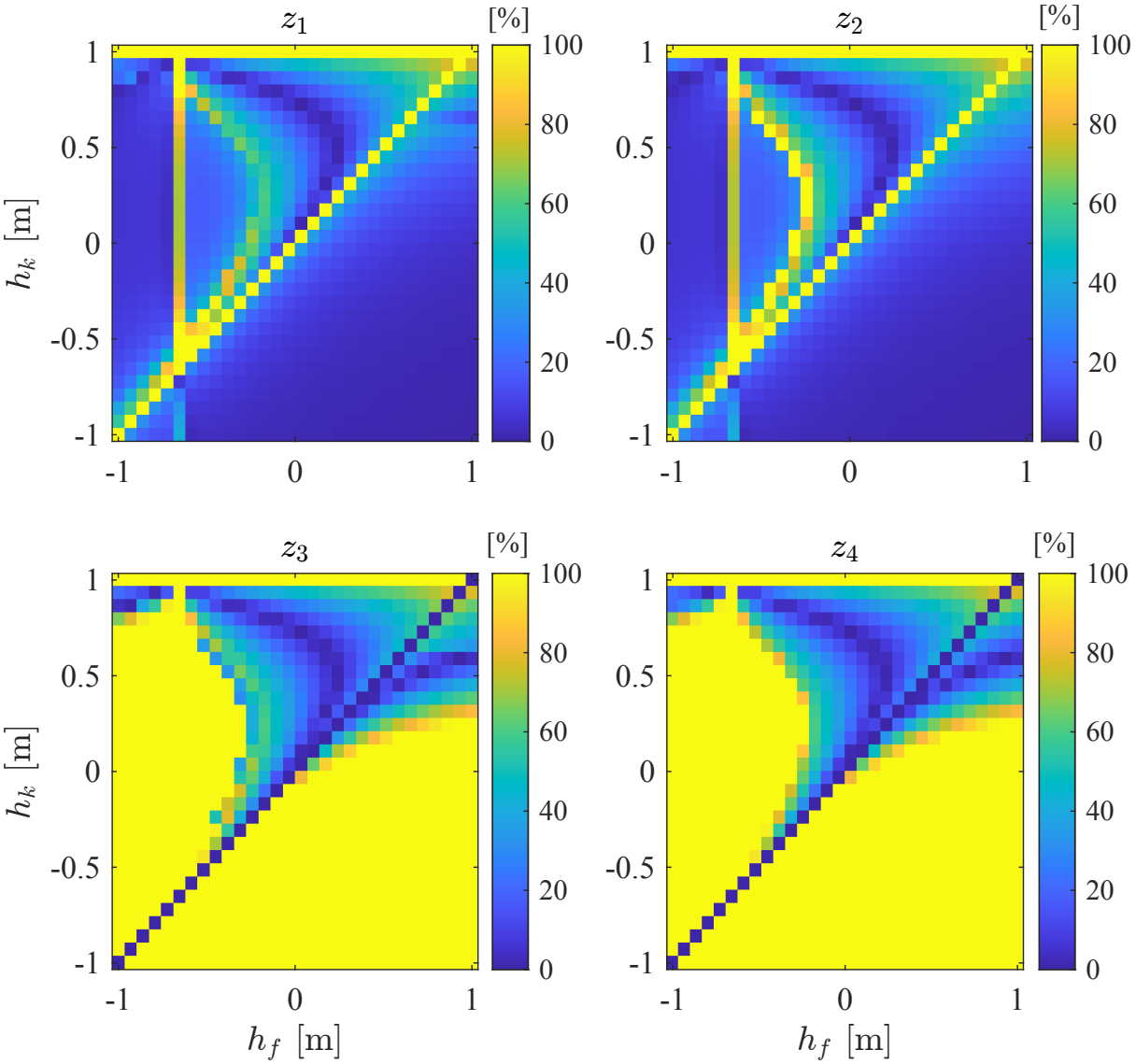

Figure 2.19: Relative error [%] between exact zeros (z_1, z_2, z_3, z_4) frequency and prediction via *ab* from the 2-Dof model of Figure 2.10.

The prediction is remarkably accurate. The first pair of zeros is indeed a mechanical feature of the 2-DoF configuration. The second pair of zeros, associated with tilt, cannot be predicted using *ab*. Its location is geometry-dependent and influenced by the sensor's trajectory.

To confirm this, it could be interesting to

- Fit a circular arc to the sensor's path, i.e, the path followed by the point $p(x, z)$ where the sensor is placed,
- Compare the predicted frequency $\sqrt{g/R}$ to the observed zero.

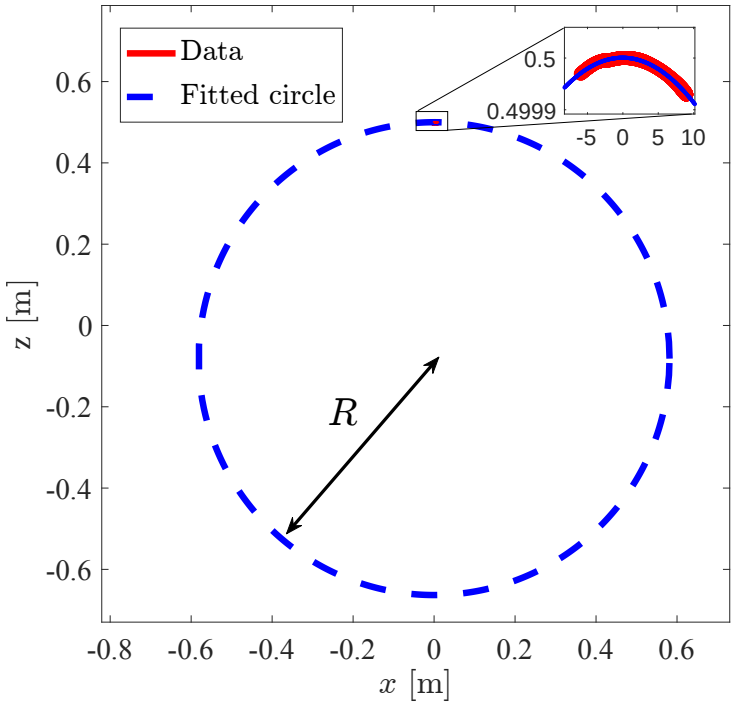

Figure 2.20: Fitted circle of radius R and obtained from the data (x, z) of a temporal simulation.

The prediction can be see in Figure **??** and is accurate. The second pair of zeros originates well from tilt-induced geometry.

Now, it remains to be studied whether the relative position of the inertial sensor can influence the location of the system's zeros in a way that is consistent with the observations made in Section 2.4. Specifically, it aims to investigate whether the same logic regarding zero placement applies in the more complex 2-DOF case.

- When the sensor is placed above the Center of Rotation (CoK), the resulting zero tends to exhibit non-minimum phase behavior dominated by tilt coupling.
- When the sensor is located below the CoK, the system's 2-DOF nature becomes more significant, and non-minimum phase characteristics may still arise due to interaction between tilt and translational dynamics.

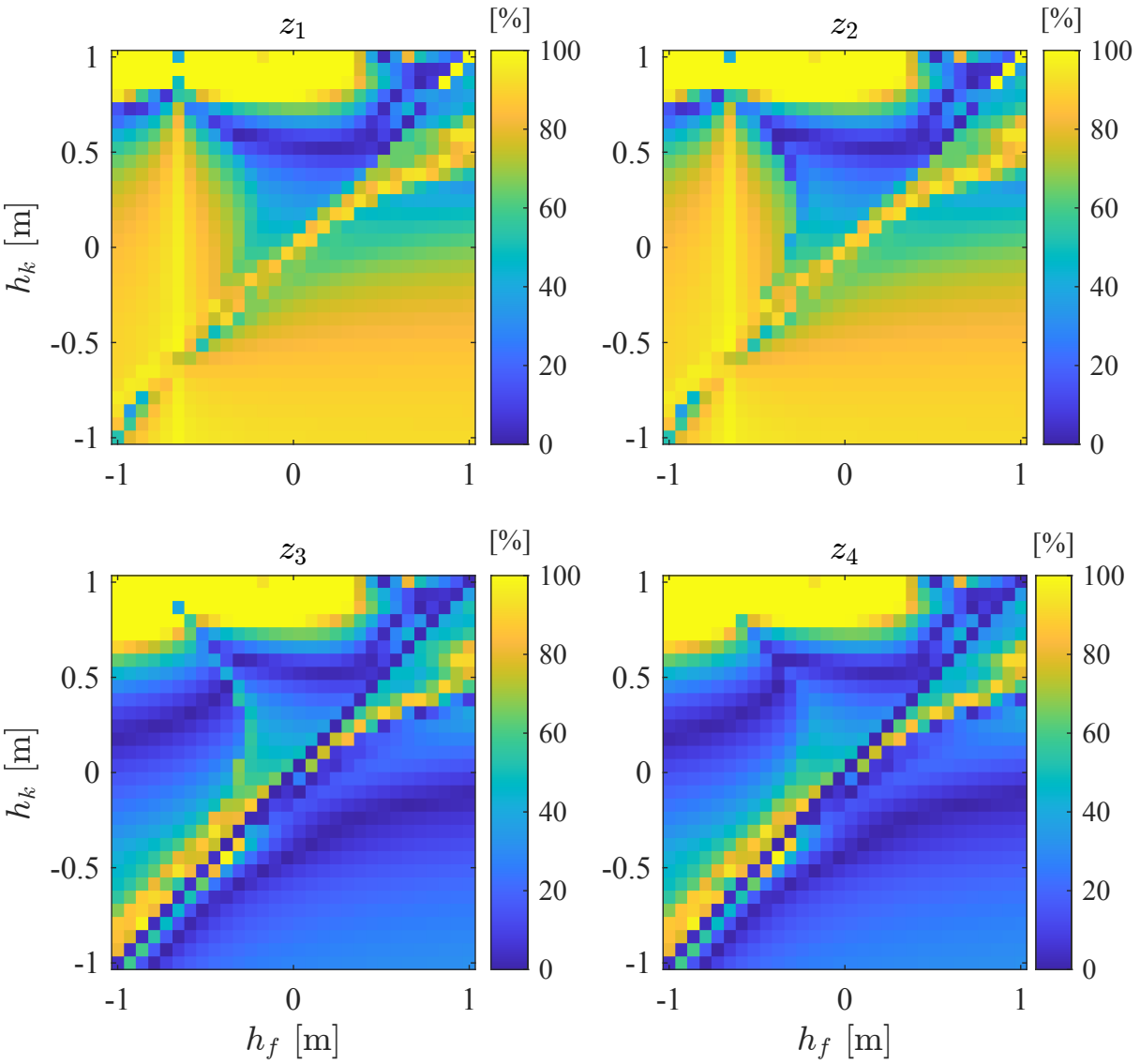

Figure 2.21: Relative error [%] between exact zeros (z_1, z_2, z_3, z_4) frequency and prediction via R from the 2-Dof model of Figure 2.10.

To explore this, the real part of the system zeros is analyzed as a function of key geometric parameters, namely the actuator height h_f and spring attachment height h_k, while fixing the sensor position either above or below the platform. The following observations can be made:

- There is no sharp boundary separating tilt-dominated and translation-dominated regimes.
- Even in the *sensor-below* configuration, tilt coupling can remain significant and influence the location of the zero.

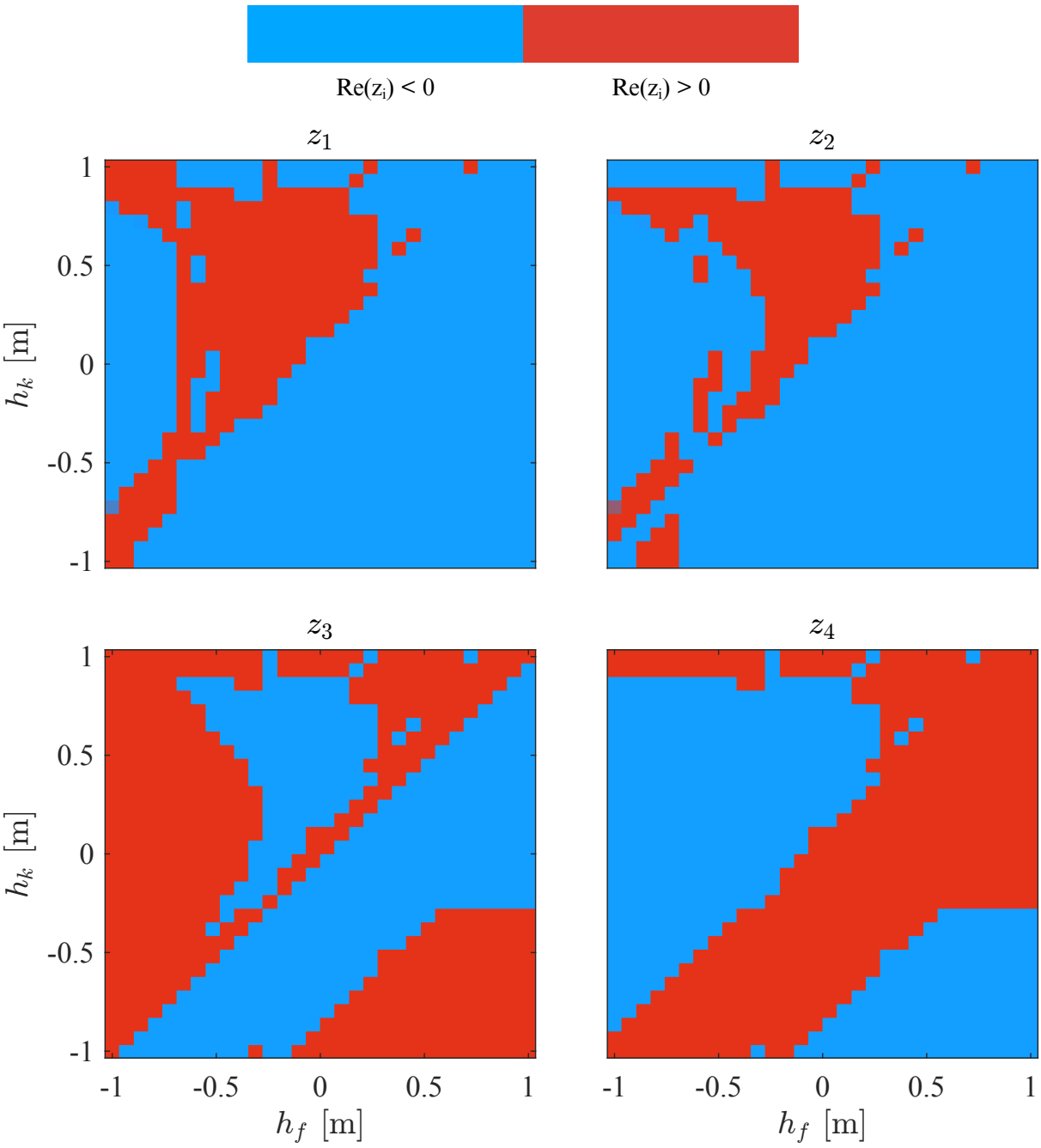

Figure 2.22: Real part of the transmission zero as a function of system geometry.

2.5.6 Conclusion

As demonstrated throughout this section, the nature of the transmission zero in a two-degree-of-freedom system is not straightforward to predict. Its characteristics result from a complex interaction between rotational tilt and translational motion, and these effects cannot always be clearly separated. As a consequence, non-minimum phase behavior is present across a wide range of configurations, and analyzing the zeros independently does not always provide a distinct interpretation.

To mitigate the presence of non-minimum phase zeros or to shift them to lower frequencies, the following design strategies can be considered

- Increase the radius of curvature of the sensor's trajectory, thereby reducing the influence of tilt.
- Maximize the mechanical decoupling between the actuator and the center of rotation.

In practice, ensuring that the sensor's trajectory is as close to purely horizontal as possible, i.e., minimizing tilt while remaining near the CoK helps reduce the adverse effects of non-minimum phase zeros. However, it should be noted that these conclusions are based on theoretical modeling, and experimental validation remains necessary to confirm these results.

Chapter 3

Experimental

3.1 Objective

This chapter aims to experimentally validate the theoretical results presented earlier concerning the pendulum system. Specifically, it investigates how the position of an inertial sensor along the pendulum affects the transfer function, with a particular focus on the emergence and nature of transmission zeros.

3.2 Methodology

An experimental setup was assembled using available resources in the Precision Mechatronics Laboratory.

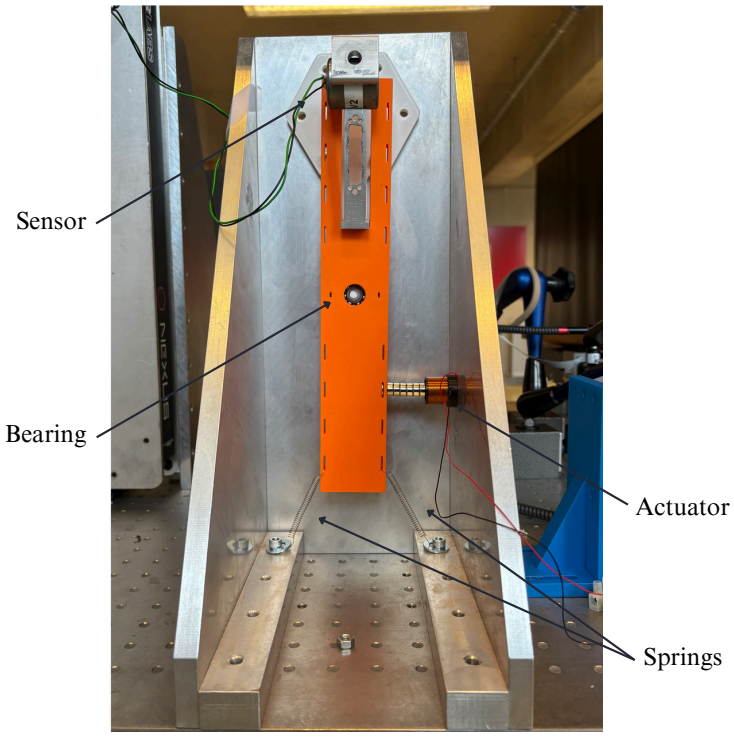

Figure 3.1: Setup showing a pendulum and an inverted pendulum equipped with an inertial sensor.

To ensure precise and repeatable sensor positioning, a custom 3D-printed part incorporating a ball bearing was used to form the pivot between the pendulum (also printed) and the supporting frame. The system is actuated via a voice-coil actuator: a wound coil generates a magnetic force proportional to the input current, which interacts with permanent magnets mounted on the pendulum, allowing controlled excitation of the structure.

The primary measurement device is a horizontal geophone, which provides a voltage proportional to relative velocity. It is connected to a voltage amplifier to reduce the influence of electrical noise introduced by the acquisition system (MicroLabBox). In parallel, a laser displacement sensor is employed to measure the absolute angular displacement $\theta(t)$ of the pendulum, serving as a clean reference for identifying poles and zeros in the system's transfer function.

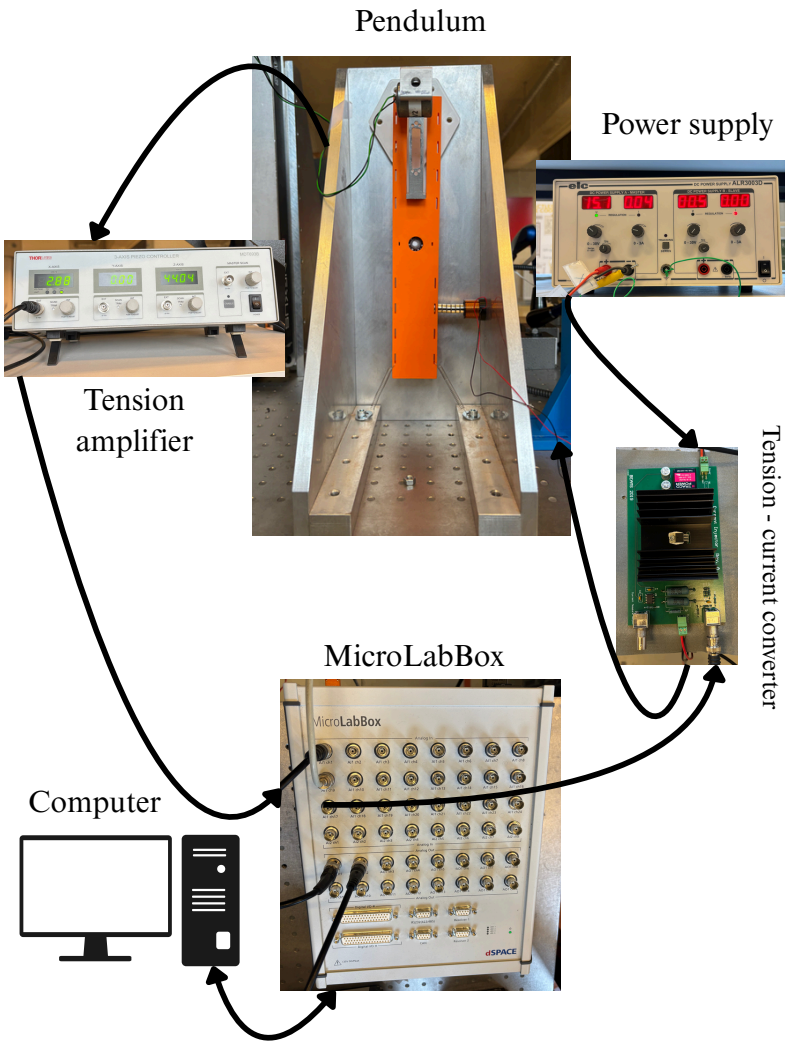

Figure 3.2: Schematic showing the connections between devices in the experimental setup.

The geophone used is a GS-11D [6], a compact velocity sensor widely used in seismic and vibration applications. It operates according to a mass–spring–damper principle, where a coil attached to an inertial mass moves within a magnetic field. The output voltage is proportional to the relative velocity between the mass and its support: $\dot{y}(t) = \dot{x}_m(t) - \dot{x}(t)$. This yields a transfer function analogous to that presented in Section 2.1, optimized for sensitivity in the velocity domain.

Parameter	**Value [units]**
Number of turns per coil	3680
Wire diameter	0.06 [mm]]
Sensitivity	32 [V/(m/s)]
Maximum current I_{max}	90 [mA]
Total weight	[0.11 kg]
Inertial mass	[0.018 kg]
Stiffness	24 [N/m]
Damping ratio	0.50
Corner frequency	4.5 [Hz]
Coil internal diameter	25 [mm]
Coil external diameter	27.9 [mm]
Transduction constant (per coil)	25 [N/A]
Electrical resistance	2 [kΩ]

Table 3.1: Characteristics of the Geophone GS-11D [6]

The electromechanical dynamics of the GS-11D can be modeled using the following coupled equations:

$$m\ddot{x}_m + c(\dot{x}_m - \dot{x}) + k(x_m - x) + Ti = 0, \tag{3.1}$$

(3.2)

$$L\frac{di}{dt} - T(\dot{x}_m - \dot{x}) + Ri = 0, \tag{3.3}$$

where T is the transduction constant and i is the induced current. This configuration causes the geophone to behave like a high-pass filter with a typical corner frequency near 4.5 Hz. At higher frequencies, the output becomes approximately proportional to ground velocity, confirming the validity of the ideal inertial model under those conditions.

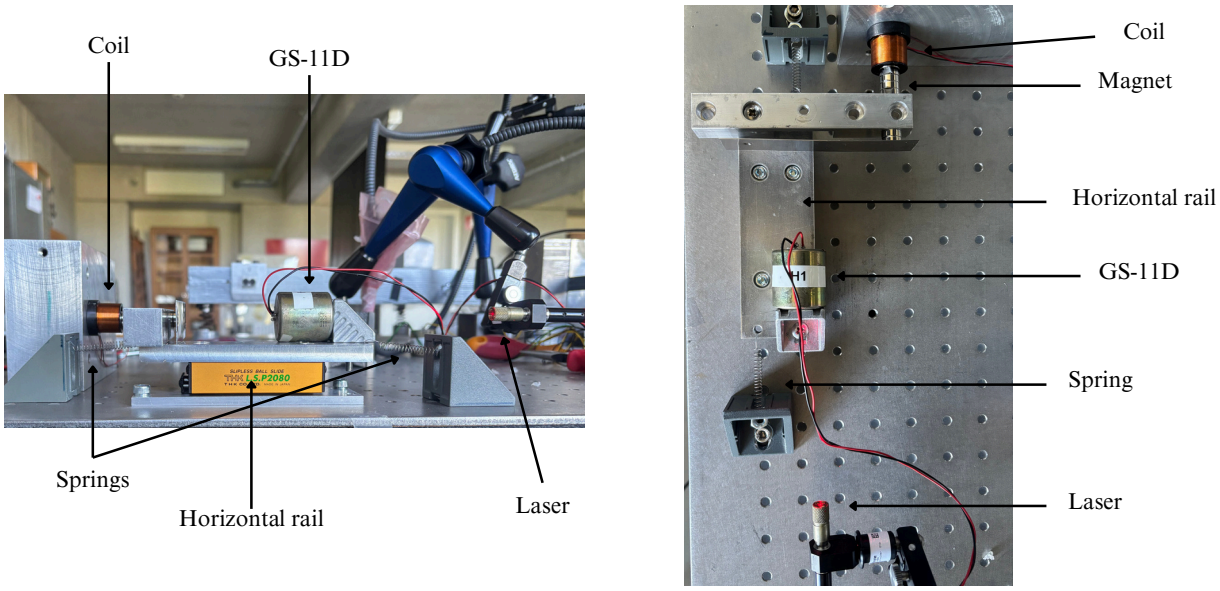

(a) Face view. (b) Top view.

Figure 3.3: Geophone mounted on a horizontal rail and suspended by two springs. A laser sensor tracks its displacement.

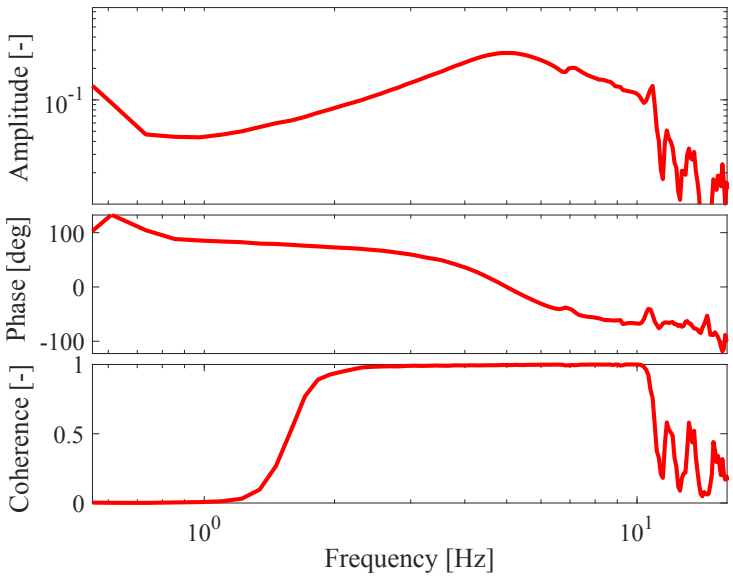

Figure 3.4: Transfer function of the GS-11D output relative to the displacement of its support, as shown in Figure 3.3b.

3.2.1 Simscape model

To aid the interpretation of poles and zeros in the transfer function, a Simscape model was created in parallel. The simulated system replicates the pendulum described in Section 2.4, using real physical dimensions and mass values. The damping and stiffness parameters were tuned to match the behavior observed in the physical setup.

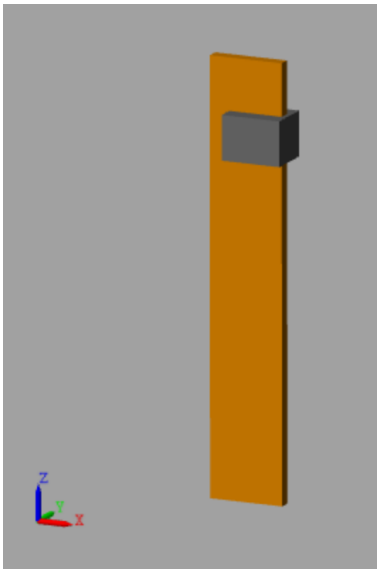

(a) Simscape implementation.

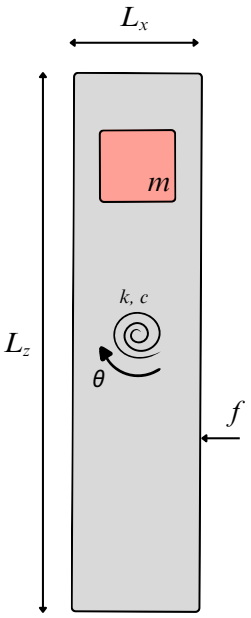

(b) Schematic representation.

Figure 3.5: Reference model used for comparing simulation results with physical experiments. The geophone is highlighted in pink.

Symbol	Description	Value [unit]
M	Mass of the pendulum structure	0.20 [kg]
m	Mass of the sensor and its support	0.71 [kg]
k_{Rz}	Rotational stiffness of the pendulum	77.1 [N/m]
c_{Rz}	Rotational damping coefficient	$0.4e-3$ [N/(m/s)]
L_x	Vertical length of the pendulum	0.05 [m]
L_z	Horizontal extension of the pendulum	0.30 [m]

Table 3.2: Physical parameters of the pendulum system.

With the setup prepared, measurements were taken for two distinct configurations. First, the inertial sensor was placed above the center of rotation (i.e., $R > 0$), where the system is expected to exhibit a non-minimum phase zero. Subsequently, the sensor was moved below the axis of rotation, and the response was analyzed as a function of the sensor's position, thereby modifying the radius of curvature.

3.3 Results

3.3.1 Theoretical validation of expected performance

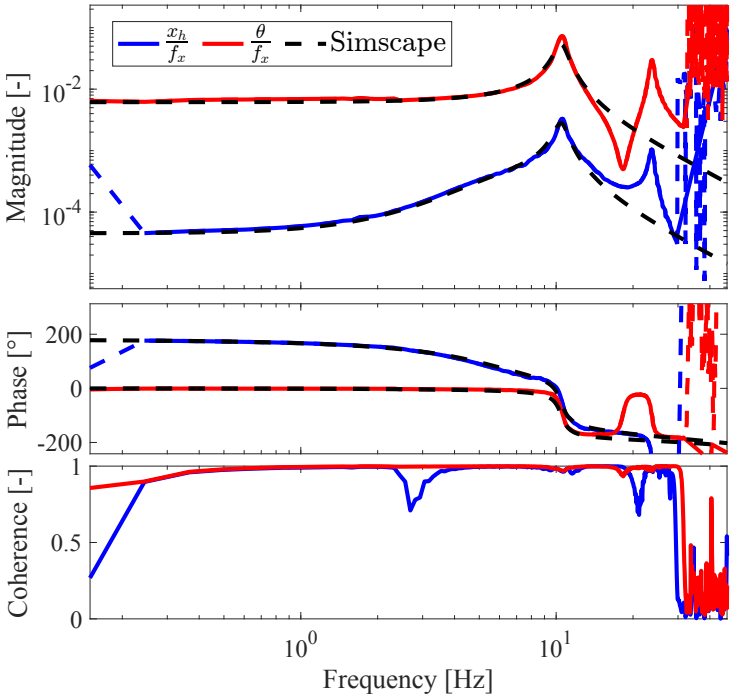

Figure 3.6: Transfer functions for the sensor placed 5.5 cm **above** the center of rotation.

In Figure 3.6:

- The red curve shows the transfer function from actuator input to the absolute angular displacement $\theta(t)$, measured by the laser sensor. A clear resonance peak corresponds to the fundamental mode of the pendulum. Simscape simulation results, when overlaid, help identify higher-order dynamics arising from structural imperfections (e.g., out-of-plane motion or flexibility).
- The blue curve represents the transfer function from actuator input to the inertial sensor output. A phase drop near 4.5 Hz indicates the influence of the geophone's own internal resonance.
- Most notably, a sharp increase in magnitude between 2–3 Hz without a corresponding phase shift is consistent with the presence of a non-minimum phase zero, as predicted theoretically.

The experiment was then repeated with the sensor placed **below** the center of rotation ($R < 0$), which corresponds to a configuration expected to yield a minimum-phase behavior.

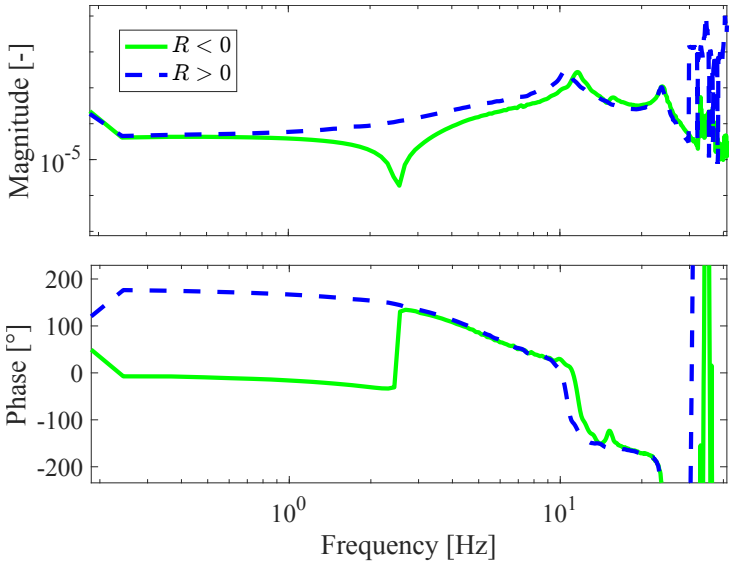

Figure 3.7: Comparison of transfer functions with the sensor placed above ($R > 0$) and below ($R < 0$) the center of rotation.

This comparison illustrates how the sign of R influences the nature of the system's zero:

- $R > 0$: the zero is non-minimum phase (sensor above pivot),
- $R < 0$: the zero becomes minimum phase (sensor below pivot).

3.3.2 Comparison with theoretical predictions

Finally, a sweep of sensor positions R was performed, and the experimentally observed zero frequencies were compared to theoretical predictions. Results are shown in Figure 3.8.

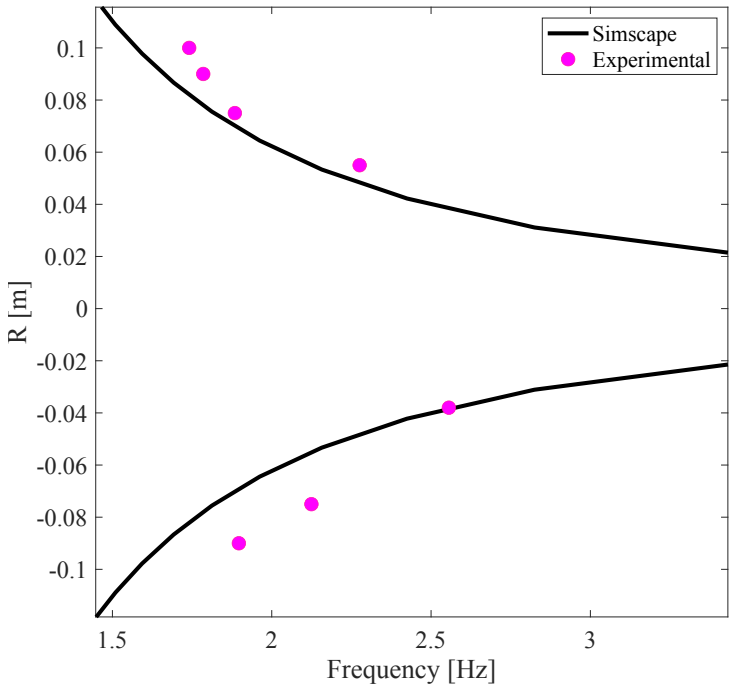

Figure 3.8: Comparison of experimental and theoretical zero frequencies as a function of sensor position R.

The strong agreement between experimental and theoretical results confirms the accuracy of the model. As expected, increasing the distance from the rotation center causes the zero frequency to shift lower. This confirms the predicted transition between minimum-phase and non-minimum-phase behavior as the sensor crosses the center of rotation.

Chapter 4

IGOR

This chapter introduces the experimental platform IGOR (Isolated Ground Optical Rig), used for control design and validation. IGOR was specifically developed to study advanced low-frequency vibration isolation techniques and has also been used to test various precision instruments, such as a gravimeter. It consists of a hybrid isolation structure that combines both passive and active elements.

The goal of the experiments is to address the challenges posed by the system's dynamic behavior, particularly the presence of non-minimum phase zeros, which complicate control design. To improve system performance and robustness, a mechanical decoupling strategy is proposed. This strategy involves modifying the structural configuration to reduce coupling between degrees of freedom, thereby improving the decoupling quality factor, denoted R. This chapter begins with a description of the platform's physical structure, followed by an overview of the sensing and actuation components.

4.1 Overview of the IGOR platform

The IGOR platform features an active isolation stage consisting of a 157 kg hexagonal table supported by three custom-designed Yuanda isolators. These isolators incorporate both sensors and actuators, enabling active control in all six degrees of freedom (translations and rotations). A schematic and a photograph of the system are shown in Fig. 4.1.

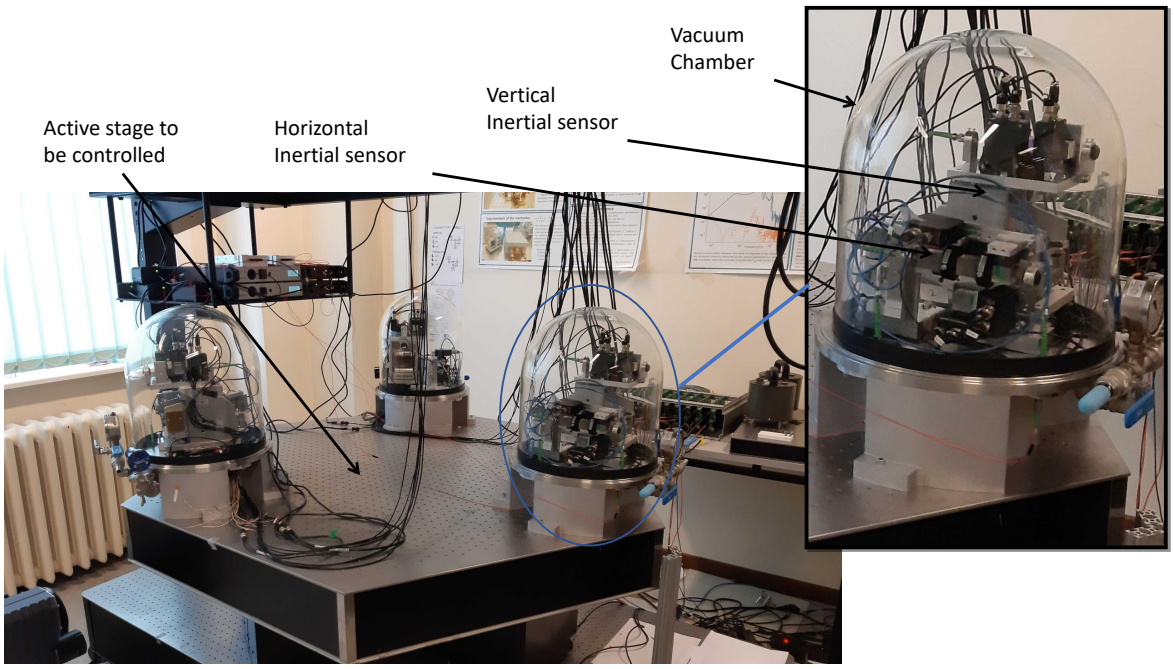

Figure 4.1: View of the IGOR platform.

In standard operation, the platform is subject to seismic and ambient vibrations. The control system is designed to minimize absolute motion within a specific low-frequency bandwidth. To enhance sensitivity in this range, high-resolution inertial sensors were installed on the table. Each sensor unit contains:

- One horizontal inertial sensor (HINS) to measure lateral motion,
- One vertical inertial sensor (VINS) for vertical displacement.

These sensors are housed in vacuum chambers to reduce air damping and ambient noise. The sensor signals are processed by a digital controller that computes the feedback control law. The control signals are then amplified and drive voice-coil actuators embedded in each isolator.

4.2 Yuanda isolators

The Yuanda isolators used in IGOR provide active vibration isolation in all six degrees of freedom. Each isolator consists of:

- Horizontal and vertical springs for mechanical compliance,
- Adaptive negative-stiffness mechanisms to reduce vertical stiffness without compromising load capacity,
- Voice-coil actuators delivering control forces in both directions.

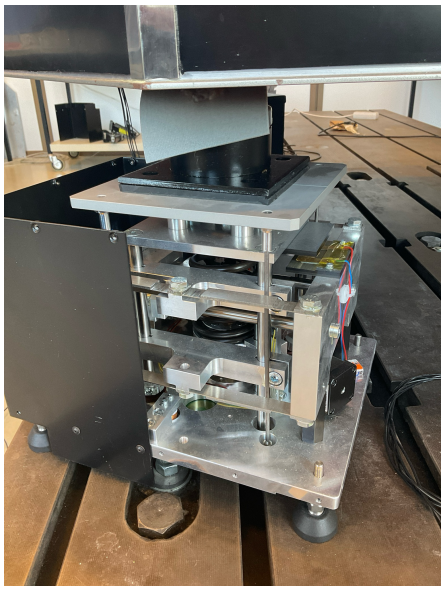

(a) Isometric view.

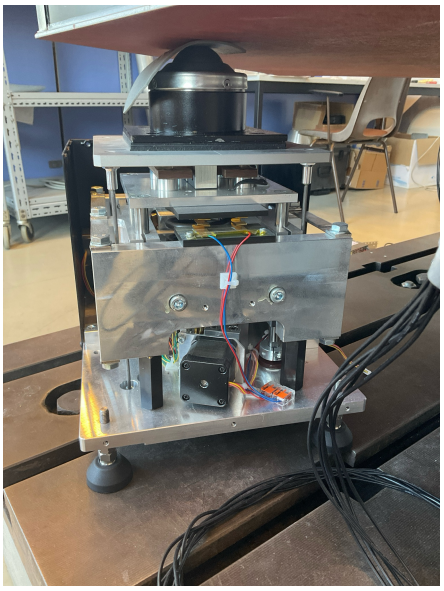

(b) Profile view.

Figure 4.2: Yuanda isolators. The negative-stiffness mechanism is visible. A spherical contact minimizes coupling between the isolators and the platform.

The force generated by each voice-coil actuator is governed by:

$$F = T_a I \tag{4.1}$$

where T_a is the actuator constant and I the input current. The actuator constants are:

- $T_a = 2.8\,\mathrm{N/A}$ for horizontal actuators,
- $T_a = 2.0\,\mathrm{N/A}$ for vertical actuators.

Each isolator supports a mass between 50 kg and 125 kg. In this study, additional dummy masses (60–70 kg) were added to reach the optimal operating range. Safety stops are installed at the center of mass. These do not engage under normal conditions but protect the platform in case of excessive motion.

4.3 Initial system configuration

Initially, the sensors were mounted on the top of the platform, as shown in Fig. 4.3. This configuration was not optimal due to tilt-horizontal coupling: the horizontal inertial sensors measured not only translational motion but also spurious rotational components caused by gravitational forces. These effects significantly degraded the control performance in the sub-Hz region. Although the control architecture relied on collocated sensing and actuation (i.e., sensor 1 and actuator 1 at the same location), the actual collocation was imperfect, leading to undesirable coupling effects.

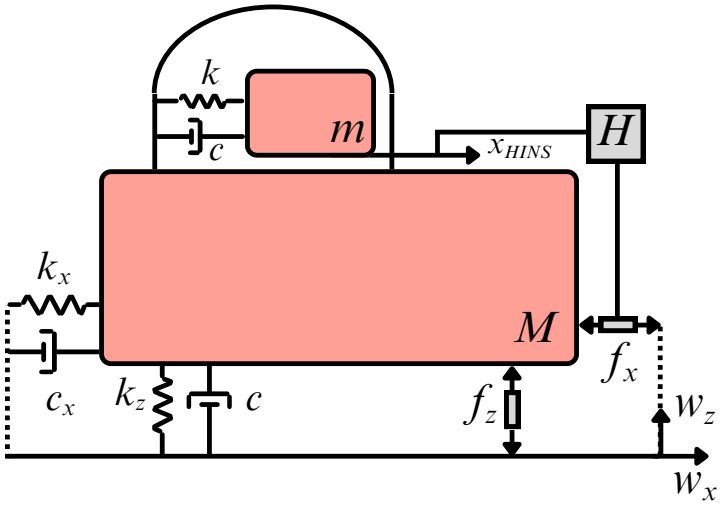

Figure 4.3: Initial positioning of horizontal inertial sensors (HINS) on the platform.

4.4 Modification strategy

To mitigate these issues, a new sensing strategy was introduced involving high-resolution relative displacement sensors from Attocube (IDS3010 series). These sensors were integrated in a sensor correction configuration, commonly used in seismic isolation systems.

Specifically:

- Inertial sensors (VINS and HINS) were repositioned on the ground to reduce tilt-translation coupling,
- Attocube interferometric sensors were mounted inside the actuator legs to measure the relative displacement between the platform and the ground.

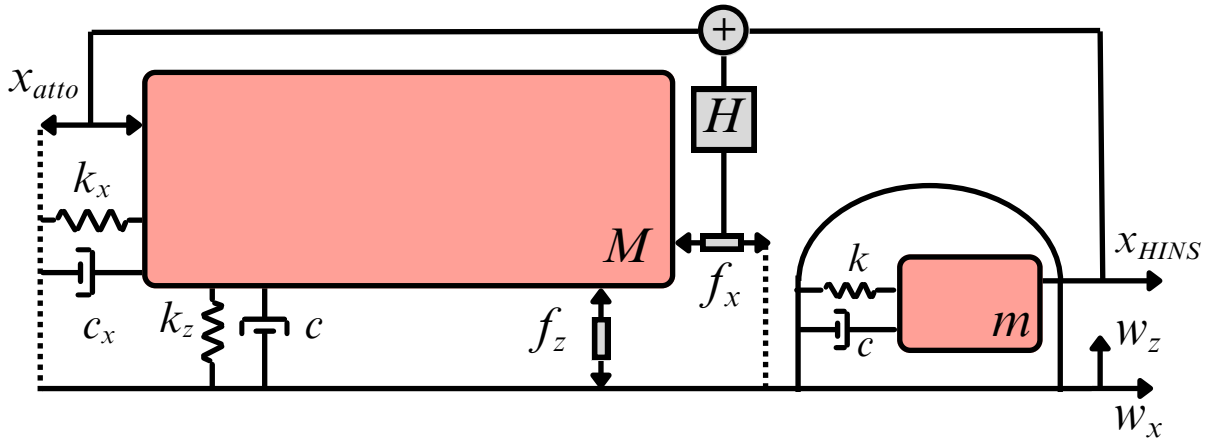

Figure 4.4: Improved sensor configuration with ground-based inertial sensors and embedded Attocube interferometers.

This hybrid sensing configuration allows the reconstruction of absolute motion by combining ground inertial measurements $x_{\text{HINS}}(t)$ with relative displacement measurements $x_{\text{atto}}(t)$, yielding:

$$x(t) = x_{\text{atto}}(t) + x_{\text{HINS}}(t)$$

provided that both signals are filtered to match their respective dynamics.

The setup benefits from custom 3D-printed PLA mounts ensuring precise alignment and minimal cross-axis sensitivity.

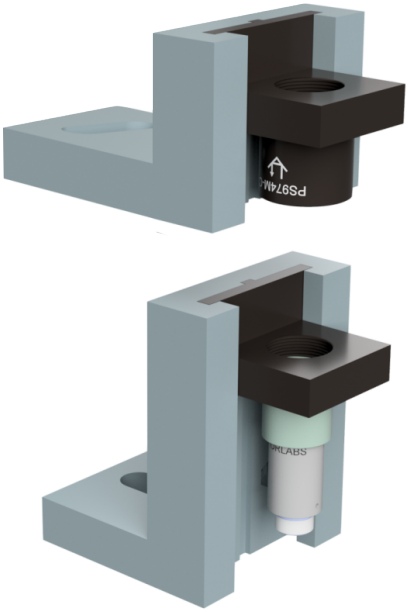

Figure 4.5: 3D-printed mounts for Attocube interferometric sensor heads.

4.5 Discussion

The improved sensor layout modifies the system's observability structure. Sensor fusion enabled by collocated Attocube and ground-based inertial sensors allows precise estimation of absolute motion. Open-loop measurements confirm the benefits:

- NMP zeros are displaced to below 0.5 Hz,
- Cross-coupling between actuation and sensing is reduced to less than 2%,
- Sensor coherence is improved in the 0.5–10 Hz band.

These results validate the design strategy and confirm the efficacy of sensor correction for low-frequency active isolation [22].

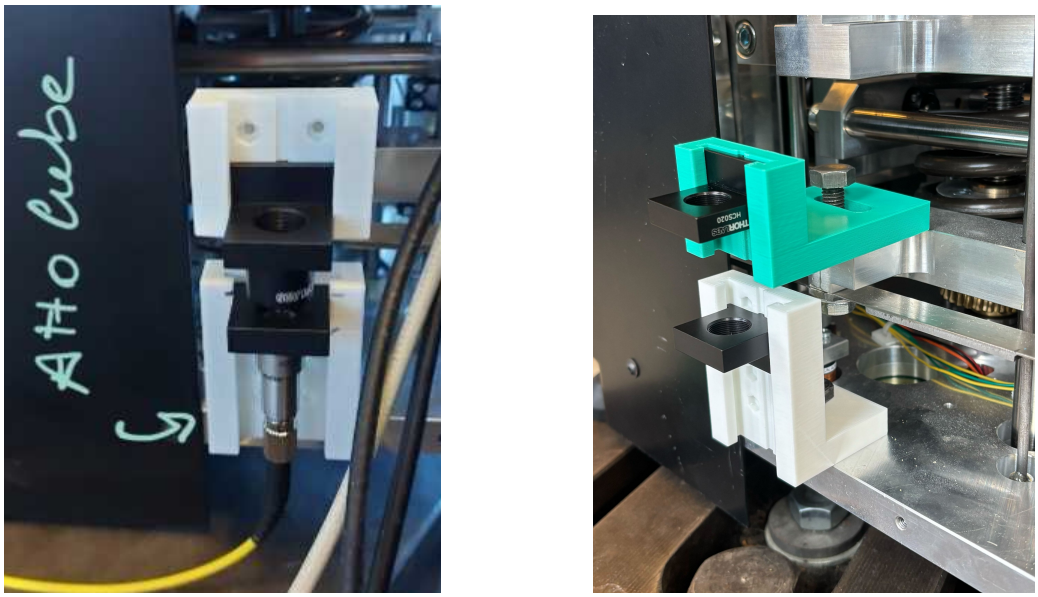

(a) Face view. (b) Isometric view.

Figure 4.6: Mounting of Attocube sensors using 3D-printed parts in the vertical direction.

As reported in [22], custom mounts were designed to integrate Attocube sensors inside the vertical actuator legs. The three sensor heads used were: Thorlabs F260FC-1550, and the Attocube D/F17 and M12/F40 heads.

Experimental transfer functions from vertical actuators to vertical relative motion sensors showed strong coherence. The estimated mechanical coupling from vertical actuation to non-collocated vertical sensors was 1.92% across all heads. Coupling from horizontal actuation to vertical sensors was 1.49%, except for the M12/F40 head which showed only 0.40%, indicating superior decoupling.

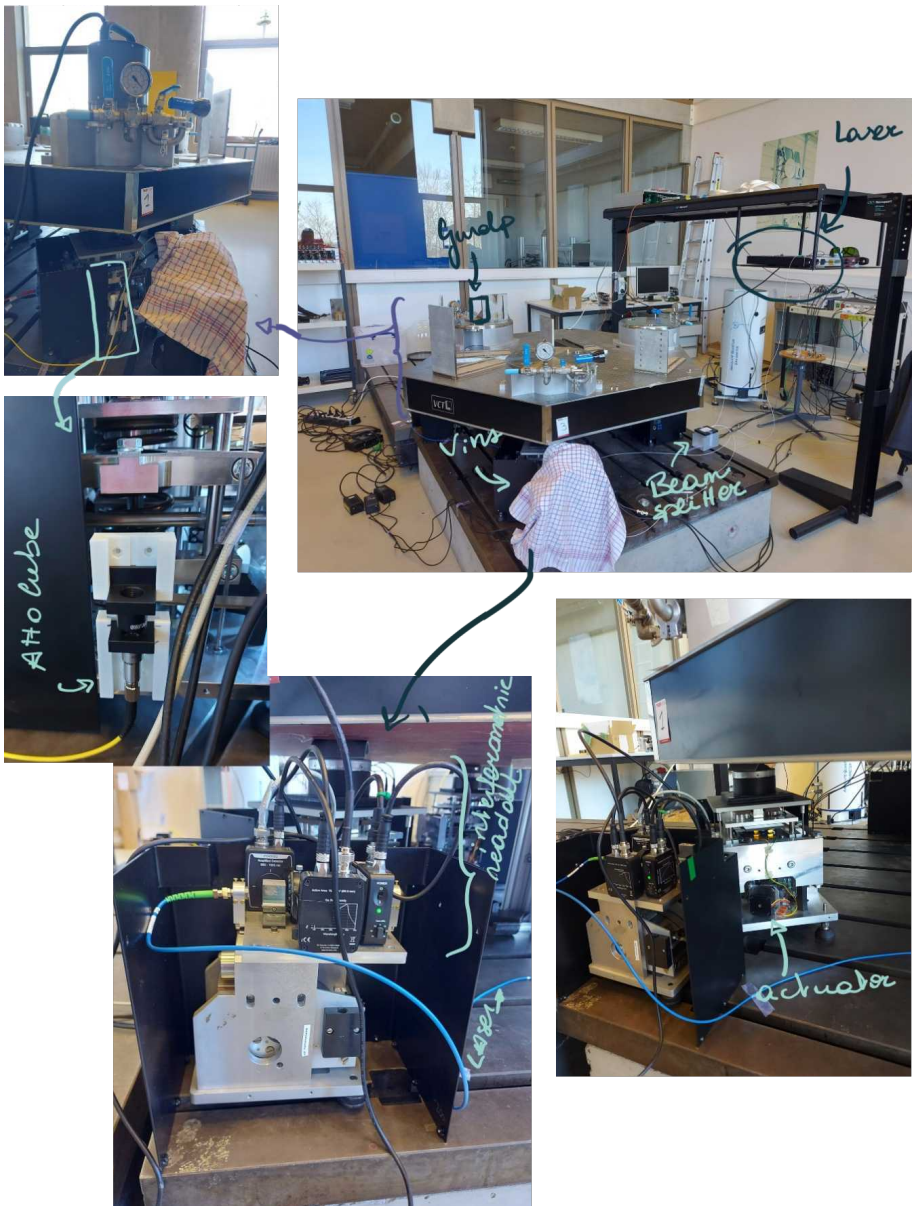

Figure 4.7: Updated IGOR setup after sensor correction implementation.

Chapter 5

Conclusions and further work

This thesis has addressed the fundamental problem of non-minimum phase behavior in active seismic isolation platforms used in gravitational wave detectors. Through a combination of theoretical modeling, frequency-domain analysis, and experimental validation, it has demonstrated that the geometry of the system particularly the relative position of the actuator, spring, and inertial sensor plays a key role in the appearance of non-minimum phase zeros. These zeros fundamentally constrain the bandwidth and robustness of feedback controllers and thus limit the performance of isolation systems in critical applications.

A key insight from this work is that such zeros often emerge from structural and sensor-actuator couplings rather than from sensor dynamics alone. Analytical derivations and parametric studies showed that the location of these zeros can be partially predicted based on geometric relationships such as the radius of curvature of the sensor path or decoupling distances. Moreover, the identification of a second, geometry-induced non-minimum phase zero beyond the classical tilt-zero emphasizes the necessity of a full-system modeling approach rather than simplistic approximations.

The experimental validation, conducted using a simplified pendulum system and simulated on a Simscape platform, confirms the theoretical predictions and highlights the practical importance of sensor placement. The results show that careful design decisions can significantly reduce the impact of adverse dynamic behaviors. These insights are not only valuable for gravitational wave detectors but are broadly applicable to any precision engineering system that employs active vibration control, such as semiconductor lithography stages, quantum measurement platforms, or even space-based optical instruments.

Looking ahead, several avenues for further research and development are proposed

- **Real-time control implementation:** Develop and test advanced feedback control strategies in real-time environments using the theoretical insights provided here, particularly focusing on robust and optimal control in the presence of multiple non-minimum phase dynamics.
- **Extension to full 6-DoF systems:** While this thesis focused primarily on 1- and

2-DoF systems, future work could extend the methodology to full six-degree-of-freedom platforms. This would allow for a more complete understanding of cross-axis couplings and complex dynamic modes in real-world systems.

- **Experimental deployment on advanced platforms:** The concepts developed in this work can be directly applied and further tested on advanced platforms such as IGOR or even in prototype configurations of the Einstein Telescope or LISA.

In conclusion, this thesis contributes a detailed understanding of how structural geometry and sensor placement affect the control limitations of seismic isolation platforms. It provides both theoretical tools and practical guidelines for engineers and physicists working on ultra-sensitive instrumentation. By deepening our knowledge of these dynamics and offering design strategies to mitigate their impact, this work lays the foundation for next-generation active isolation systems capable of supporting groundbreaking discoveries in astrophysics and beyond.

Bibliography

[1] Andrea Cattaneo : Les générations d'observateurs d'ondes gravitationnelles, 2017. Accessed: 2025-05-07.

[2] LIGO Scientific Collaboration : Ligo laboratory website, 2025. Accessed multiple times between Feb and May of 2025.

[3] F. Acernese et al. : Advanced virgo: a second-generation interferometric gravitational wave detector. *Classical and Quantum Gravity*, 32(2):024001, 2015.

[4] KAGRA Collaboration : Overview of kagra: Detector design and construction history. *Progress of Theoretical and Experimental Physics*, 2021(5):05A101, 2021. [CrossRef], [Google Scholar].

[5] P. et al. Amaro-Seoane : Laser interferometer space antenna. *arXiv preprint arXiv:1702.00786*, 2017.

[6] Christophe Collette, Lionel Fueyo-Roza et Mihaita Horodinca : Prototype of a small low noise absolute displacement sensor. *IEEE Sensors Journal*, 13(12):4725–4732, 2013.

[7] Albert Einstein : Die grundlage der allgemeinen relativitätstheorie. *Annalen der Physik*, 354(7):769–822, 1916.

[8] M. Maggiore : *Gravitational Waves: Volume 1: Theory and Experiments*. Oxford University Press, 2008.

[9] P. Saulson : *Fundamentals of Interferometric Gravitational Wave Detectors*. World Scientific, 1994.

[10] B. S. Sathyaprakash et Bernard F. Schutz : Physics, astrophysics and cosmology with gravitational waves. *Living Reviews in Relativity*, 12(1):2, 2009.

[11] B. P. Abbott *et al.* : Observation of gravitational waves from a binary black hole merger. *Physical Review Letters*, 116(6):061102, 2016.

[12] J. Aasi *et al.* : Advanced ligo. *Classical and Quantum Gravity*, 32(7):074001, 2015.

[13] G. Hobbs *et al.* : The international pulsar timing array project: using pulsars as a gravitational wave detector. *Classical and Quantum Gravity*, 27(8):084013, 2010.

[14] J. Weber : Detection and generation of gravitational waves. *Physical Review*, 117: 306, 1960.

[15] D. et al. Martynov : Sensitivity of the advanced ligo detectors at the beginning of gravitational wave astronomy. *Physical Review D*, 93(11):112004, 2016.

[16] M. et al. Punturo : The einstein telescope: a third-generation gravitational wave observatory. *Classical and Quantum Gravity*, 27(19):194002, 2010.

[17] D. et al. Reitze : Cosmic explorer: The u.s. contribution to next-generation ground-based gravitational-wave observatories. *Bulletin of the American Astronomical Society*, 51(7), 2019.

[18] K. Somiya : Detector configuration of kagra: The japanese cryogenic gravitational-wave detector. *Classical and Quantum Gravity*, 29(12):124007, 2012.

[19] H. Grote et the GEO600 Team : The geo 600 status. *Classical and Quantum Gravity*, 27(8):084003, 2010.

[20] G. F. Franklin, J. D. Powell et A. Emami-Naeini : *Feedback Control of Dynamic Systems*. Pearson, 8th édition, 2019.

[21] F. Matichard et al. : Seismic isolation of advanced ligo: Review of strategy, instrumentation, and performance. *Classical and Quantum Gravity*, 32(18):185003, 2015.

[22] Thomas Giordano et Anthony Amorosi : Attocube loan kit report. Rapport technique, Precision Mechatronics Laboratory, University of Liège, April 2025. Internal report on IGOR platform integration and sensor correction.

[23] G. M. Harry et the LIGO Scientific Collaboration : Advanced ligo: the next generation of gravitational wave detectors. *Classical and Quantum Gravity*, 27(8):084006, 2010.

[24] F. Matichard et al. : Advanced ligo two-stage twelve-axis vibration isolation and positioning platform. part 1: Design and production overview. *Precision Engineering*, 40:273–286, 2015.

[25] G. Cella et al. : The effect of tilt on seismic inertial sensors. *Nuclear Instruments and Methods in Physics Research Section A*, 432(3):482–492, 1999.

[26] Alexandre Le Tiec et Jérôme Novak : Theory of gravitational waves. *In World Scientific Review Volume*, pages 1–40. World Scientific, Meudon Cedex, France, 2016. Chapter 1, LUTH, Observatoire de Paris, PSL Research University.

[27] F. Matichard, B. Lantz, R. Mittleman, K. Mason et J. Kissel : Seismic isolation of advanced ligo: Review of strategy, instrumentation and performance. *Classical and Quantum Gravity*, 32(18):185003, 2015. Pre-Print version available at LSU Scholarly Repository.

[28] Ilaria Taurasi : Inverted pendulum studies for seismic attenuation. Rapport technique, California Institute of Technology, Pasadena, CA, USA, 2005. SURF Final Report, LIGO-T060048-00-R.

[29] B. Lantz, R. Schofield, B. O'Reilly, D. E. Clark et D. DeBra : Requirements for a ground rotation sensor to improve advanced ligo. *Bulletin of the Seismological Society of America*, 99(2B):980–989, May 2009.

[30] B.P. et al. Abbott : Observation of gravitational waves from a binary black hole merger. *Physical Review Letters*, 116(6):061102, 2016.

[31] J.P.W. et al. Verbiest : The international pulsar timing array: First data release. *Monthly Notices of the Royal Astronomical Society*, 458(2):1267–1288, 2016.

[32] A. et al. Buikema : Sensitivity and performance of the advanced ligo detectors in the third observing run. *Physical Review D*, 102(6):062003, 2020.

[33] G. et al. Cella : The effect of tilt on seismic inertial sensors. *Nuclear Instruments and Methods in Physics Research Section A*, 432(3):482–492, 1999.

[34] S. Skogestad et I. Postlethwaite : *Multivariable Feedback Control: Analysis and Design*. Wiley, 2005.

[35] A. Le Tiec et J. Novak : Theory of gravitational waves. *World Scientific Review Volume*, pages 1–40, 2016.

[36] S. Danilishin et F. Khalili : Quantum measurement theory in gravitational-wave detectors. *Living Reviews in Relativity*, 15(1):5, 2012.

[37] S. et al. Hild : Einstein telescope design report. Rapport technique, ET Collaboration, 2020. ET-0106C-10.

[38] J. Thorpe, P. McNamara et J. Trigo-Rodriguez : Lisa pathfinder and lisa: Preparing for precision interferometry in space. *In Proceedings of the 9th LISA Symposium*, 2011.

[39] European Space Agency : Lisa mission website, 2020. https://www.cosmos.esa.int/web/lisa.

[40] The LIGO Scientific Collaboration : Enhanced sensitivity of the ligo gravitational wave detector by using squeezed states of light. *Nature Photonics*, 7(8):613–619, 2013.

[41] H. Grote et the LIGO Scientific Collaboration : First long-term application of squeezed states of light in a gravitational-wave observatory. *Physical Review Letters*, 110(18):181101, 2013.

[42] T. Uchiyama *et al.* : Thermal noise reduction and cryogenic systems for the kagra interferometer. *Physics Procedia*, 61:633–639, 2014.

[43] M. Tinto et S. V. Dhurandhar : Time-delay interferometry. *Living Reviews in Relativity*, 17(1):6, 2014.